Doctoral Dissertation

Studies on Novel Environment-Friendly Inorganic Pigments

（環境に優しい新規無機顔料に関する研究）

January 2021

Ryohei Oka

Department of Chemistry and Biotechnology

Graduate School of Engineering

Tottori University

Preface

The studies presented in this thesis were carried out under the supervision of Professor Dr. Toshiyuki Masui at Applied Chemistry Course, Department of Chemistry and Biotechnology, Graduate School of Engineering, Tottori University during 2018–2021. The present study has been partially supported by the Japan Society for the Promotion of Science (JSPS) research fellowship (No. 201823369) from 2018 to 2021.

The object of this thesis is to develop novel environmentally friendly inorganic pigments and to reveal the coloring mechanism of them. The author wishes that the findings and the knowledge obtained from this work would be able to contribute to further development and design of novel environmentally friendly inorganic pigments.

Ryohei Oka

Department of Chemistry and Biotechnology

Graduate School of Engineering

Tottori University

4-101 Minami, Koyama-cho, Tottori 680-8552, Japan

January 2021

Contents

Chapter 1

General Introduction

1.1 Inorganic warm-colored pigments

Almost all objects around us are colored in a variety of colors. Color not only gives objects aesthetic appearances, but also play a role in visually communicating information such as safety colors and warning signs. One of the materials that color objects is pigment. Pigments are powders exhibiting colors that are insoluble or poor-soluble in water and organic solvents. They selectively absorb a part of the visible light and exhibit the complementary colors of the absorbed light.

Pigments fall into the general classification of organic or inorganic ones. Inorganic pigments are typically applied in a wide range of products such as paints, ceramics, and inks, because they possess high hiding power and thermal resistance compared to organic pigments.[1,2] In particular, there is a great demand for warm-colored (i.e., orange or red) inorganic pigments. Some orange and red pigments such as molybdate orange ($PbCrO_4 \cdot PbMoO_4 \cdot PbSO_4$), lead oxide red ($Pb_3O_4$), mercuric sulfide red (HgS), and cadmium red (CdS·CdSe) have been popularly used as industrial inorganic color materials. However, these pigments contain elements (e.g., Cr, Pb, Hg, Cd, and Se) that are toxic to the environment and the human body. Accordingly, the use of the conventional pigments composed of these harmful elements is tended to be regulated or banned on a global scale.

In recent years, sulfides and oxynitrides such as Ce_2S_3 and $Ca_{1-x}La_xTaO_{2-x}N_{1+x}$ have attracted attention as materials exhibiting vivid colors.[3–6] However, sulfide pigments are poor in chemical stability and may cause discoloration when mixed with other pigments. For the synthesis of oxynitride pigments, harmful ammonia gas is required. In view of practical use, oxide pigments are desirable, because they have excellent chemical and thermal stabilities and toxic gas is not required for the synthesis process. Although several studies on orange and red pigments have been reported,[7–37] there are few environmentally friendly inorganic warm-colored oxide pigments which possess high performance comparable to the conventional toxic ones.

1.2 NIR-reflective pigments

Recently, the urban heat-island phenomenon has been observed around the world. The urban heat-island effect leads to the ambient temperature in an urban area being higher than that in the surrounding areas.[38] This effect often generates adverse effects such as heatstroke, discomfort, and a large consumption of electricity by air conditioners in the summer season. Natural sunlight consists of 5% ultraviolet radiation (UV; 280–400 nm), 43% visible radiation (400–700 nm) and 52% near-infrared radiation (NIR; 700–2500 nm).[39] Since the 700–1300 nm wavelength region constitutes 80% of the total energy in the NIR region, sunlight in this range plays the most important role in generating heat.[40] For this reason, it is effective to shield

NIR light in this region in order to prevent heat storage. Many studies have been reported on several colored pigments that can reflect NIR light.[15,19,41–53)]

The NIR-reflectance properties of variously colored pigments (e.g., white, yellow, and blue) are generally better than those of black pigments, because these pigments tend to reflect not only visible but also NIR light.[54,55)] However, black pigments such as carbon black basically absorb NIR as well as visible light to store heat. When the common black pigment on the outer walls and roofs of buildings absorbs sunlight, the temperature rises, and at the same time the amount of exhaust heat from the use of air conditioners increases. Additionally, the heat stored during the daytime is released at night, and this heat dissipation prevents night cooling. These phenomena promote the urban heat island. For this reason, application of NIR-reflective black pigments to road surfaces, building roofs, and exterior walls has attracted attention.[55,56)] Some compounds such as $(Fe, Cr)_2O_3$, Fe_2TiO_4, and $YMnO_3$ have been proposed to serve as NIR-reflective black pigments.[2,56–58)] However, $(Fe, Cr)_2O_3$ contains toxic chromium, and NIR-reflective properties of Fe_2TiO_4 and $YMnO_3$ are not enough. Therefore, development of new inorganic black pigments having high NIR reflective properties has been required.

1.3 Outline of this study

Based on the backgrounds mentioned above, the author studied the novel environmentally friendly inorganic warm-colored and NIR-reflective black pigments.

This thesis consists of the following five chapters.

In **Chapter 2**, the novel environmentally friendly inorganic orange pigments, $Ca_{14}(Al_{1-x})_{10}Zn_6O_{35}$ ($0 \leq x \leq 0.30$), are described. The chemical composition was optimized to produce the most vivid orange hue. Furthermore, the chemical and thermal stabilities of the present pigment were compared to those of the commercially available orange pigments.

In **Chapter 3**, the color characteristics of $(Bi_{1-x}Ta_x)_2O_{3+2x}$ ($0 \leq x \leq 0.20$) solid solutions are described, which were synthesized as novel environmentally friendly inorganic orange pigments. The relationships between the color and crystal system of these solid solutions were investigated.

In **Chapter 4**, the color characteristics of $(Li_{1-x}Na_x)_2MnO_3$ ($0 \leq x \leq 0.10$) solid solutions are described. To investigate the relationships between steric structure of $[MnO_6]$ octahedra and coloration mechanisms, the crystal structure of these solid solutions was refined by the Rietveld method using the XRD patterns.

In **Chapter 5**, $Ca_2Mn_{0.85-x}Ti_{0.15}Zn_xO_{4-x}$ ($0 \leq x \leq 0.10$) pigments were synthesized to improve the black tone color of a $Ca_2Mn_{0.85}Ti_{0.15}O_4$ pigment,[59] which was previously reported by our group but exhibited slightly reddish black color.

In **Chapter 6**, this study with main results and knowledges was totally summarized.

Chapter 2

Synthesis and Characterization of Novel Environmentally Friendly Inorganic Orange Pigments Based on $Ca_{14}Al_{10}Zn_6O_{35}$

2.1 Introduction

As mentioned in Chapter 1, development of alternative environmentally friendly inorganic orange pigments with high thermal stability has been required. Because of this situation, our research group focused on Fe^{3+} ion as an orange coloring source. Fe^{3+}-containing materials have been investigated by several researchers.[7,9,19,20,31,41,60–64] These materials absorb visible light due to the d–d transition of Fe^{3+} and the O_{2p}–Fe_{3d} charge transfer transition. However, some compounds such as (Ce, Pr, Fe)O_2, K(Zn, Fe)PO_4, and (Y, Tb)$_2$(Zr, Fe)$_2O_7$ show reddish color, because Fe^{3+} is doped into weak crystal field sites.[7,31,62] Exceptionally, Y(In, Fe)O_3 exhibits vivid orange color.[9] However, the raw material (In_2O_3) to synthesize this compound is expensive. The color of the pigments depends on the Fe^{3+} content and the coordination environment around the Fe^{3+} ions. For example, the compounds containing Fe^{3+} at high concentrations become reddish, and the absorption wavelength corresponding to the d–d transition is affected by the crystal field strength around the Fe^{3+} ions. The energy splitting of the d-orbitals becomes smaller, when the Fe^{3+} ions are doped into a cation site, of which the ionic radius is larger than that of Fe^{3+}. As a result, the optical absorption bands due to the d–d

transition shift to longer wavelength. In a contrasting situation, if a cation site with an ionic radius smaller than that of Fe^{3+} is substituted with Fe^{3+} ions, the absorption bands shift to shorter wavelengths.

$Ca_{14}Al_{10}Zn_6O_{35}$ was selected as a host material, because this compound is composed of only non-toxic elements and has chemical and thermal stabilities.[65–67] $Ca_{14}Al_{10}Zn_6O_{35}$ has been reported as a good mother for deep red emitting phosphors. In $Ca_{14}Al_{10}Zn_6O_{35}$, Mn^{4+} ions are preferentially accommodated at the Al^{3+} site to emit red light.[68] The crystal field around the Al^{3+} site is strong, because the ionic radius of Fe^{3+} (0.063 nm)[69] is larger than that of Al^{3+} (0.053 nm).[69] Accordingly, optical absorption due to the d–d transition ($^6A_1 \rightarrow {}^4E$) of Fe^{3+} should appear at shorter wavelength than those of the conventional Fe^{3+}-doped reddish materials, and it is expected that orangish color is obtained when the Fe^{3+} ions are doped into the Al^{3+} site in $Ca_{14}Al_{10}Zn_6O_{35}$. Therefore, $Ca_{14}(Al_{1-x}Fe_x)_{10}Zn_6O_{35}$ ($0 \leq x \leq 0.25$) pigments were synthesized and the composition was optimized to produce the most vivid orange hue.[70]

2.2 Experimental Procedure

2.2.1 Materials and methods

The $Ca_{14}(Al_{1-x}Fe_x)_{10}Zn_6O_{35}$ ($0 \leq x \leq 0.25$) samples were synthesized using a conventional solid-state reaction method. The starting materials were $CaCO_3$ (Wako Pure Chemical Industries Ltd., 99.5 %), $Al(OH)_3$ (Wako Pure Chemical Industries Ltd., 95.0 %), ZnO (Kishida

Chemical Co. Ltd., 99.5 %) and Fe_2O_3 (Wako Pure Chemical Industries Ltd., 99.9 %) powders. Stoichiometric amounts of each reagent were mixed in an agate mortar. The mixtures were calcined in an alumina boat at 1250 °C for 6 h under an air atmosphere. Before characterization, the samples were ground in an agate mortar.

2.2.2 Characterization

The molar ratio of metal in the samples were analyzed by X-ray fluorescence spectroscopy (XRF; Rigaku, ZSX Primus). The samples were characterized using X-ray powder diffraction (XRD; Rigaku, Ultima IV) with Cu-Kα radiation (40 kV, 40 mA). The lattice parameters and volumes were calculated from the XRD peak angles, which were refined using α-Al_2O_3 as a standard and using the CellCalc Ver 2.20 software. The morphology of the $Ca_{14}(Al_{1-x}Fe_x)_{10}Zn_6O_{35}$ ($0 \leq x \leq 0.25$) particles was observed by using field-emission-type scanning electron microscopy (FE-SEM; JEOL, JSM-6701F). The optical reflectance spectroscopy measurements of the samples were taken with a UV–Vis spectrometer (Shimadzu, UV-2550) with barium sulfate as a reference. The color properties of the samples were evaluated in terms of the CIE $L^*a^*b^*Ch^\circ$ system using a colorimeter (Konica-Minolta, CR-300). The L^* parameter indicates the brightness or darkness of a color relative to a neutral grey scale, while a^* (the red–green axis) and b^* (the yellow–blue axis) parameters express the color qualitatively. The chroma parameter (C) represents the color saturation of the pigments and is

calculated according to the following formula (2-1). The parameter $h°$ ranges from 0 to 360° and is calculated with the formula (2-2).

$$C = [(a^*)^2 + (b^*)^2]^{1/2} \quad (2\text{-}1)$$

$$h° = \tan^{-1}(b^*/a^*) \quad (2\text{-}2)$$

2.3 Results and Discussion

2.3.1 X-ray fluorescence analysis (XRF)

The sample compositions analyzed using XRF are listed in **Table 2.1**. They were almost in good agreement with the stochiometric values.

Table 2.1 Stoichiometric and analyzed composition of the $Ca_{14}(Al_{1-x}Fe_x)_{10}Zn_6O_{35}$ ($0 \le x \le 0.25$) samples

x	Stoichiometric composition	Analyzed composition
0	$Ca_{14}Al_{10}Zn_6O_{35}$	$Ca_{14}Al_{10}Zn_6O_{35}$
0.05	$Ca_{14}(Al_{0.95}Fe_{0.05})_{10}Zn_6O_{35}$	$Ca_{14}(Al_{0.95}Fe_{0.05})_{10}Zn_6O_{35}$
0.10	$Ca_{14}(Al_{0.90}Fe_{0.10})_{10}Zn_6O_{35}$	$Ca_{14}(Al_{0.90}Fe_{0.10})_{10}Zn_6O_{35}$
0.15	$Ca_{14}(Al_{0.85}Fe_{0.15})_{10}Zn_6O_{35}$	$Ca_{14}(Al_{0.84}Fe_{0.16})_{10}Zn_6O_{35}$
0.20	$Ca_{14}(Al_{0.80}Fe_{0.20})_{10}Zn_6O_{35}$	$Ca_{14}(Al_{0.79}Fe_{0.21})_{10}Zn_6O_{35}$
0.25	$Ca_{14}(Al_{0.75}Fe_{0.25})_{10}Zn_6O_{35}$	$Ca_{14}(Al_{0.74}Fe_{0.26})_{10}Zn_6O_{35}$

2.3.2 X-ray powder diffraction (XRD)

Figure 2.1 shows the XRD patterns of the synthesized $Ca_{14}(Al_{1-x}Fe_x)_{10}Zn_6O_{35}$ ($0 \le x \le 0.25$) samples. Among these samples, Fe^{3+}-doped $Ca_{14}(Al_{1-x}Fe_x)_{10}Zn_6O_{35}$ ($0.05 \le x \le 0.25$)

were obtained in a single-phase form. In the case of the non-doped $Ca_{14}Al_{10}Zn_6O_{35}$ (x = 0) sample, however, a nominal amount of CaO was detected as an impurity. In addition, the $Ca_{14}(Al_{0.70}Fe_{0.30})_{10}Zn_6O_{35}$ (x = 0.30) sample was melted and it could not be collected as a powder sample. The lattice volumes of all samples are summarized in **Table 2.2**, where the numbers in parentheses indicate standard deviations. $Ca_{14}Al_{10}Zn_6O_{35}$ forms a cubic structure with space group of $F23$.[71] The cell volume increased as the Fe^{3+} concentration was increased, indicating that some Al^{3+} ions were substituted with Fe^{3+}, because the ionic radius of Fe^{3+} (0.0645 nm)[69] is larger than that of Al^{3+} (0.0535 nm).[69] Therefore, the solid solutions based on $Ca_{14}Al_{10}Zn_6O_{35}$ were successfully synthesized in a single-phase form.

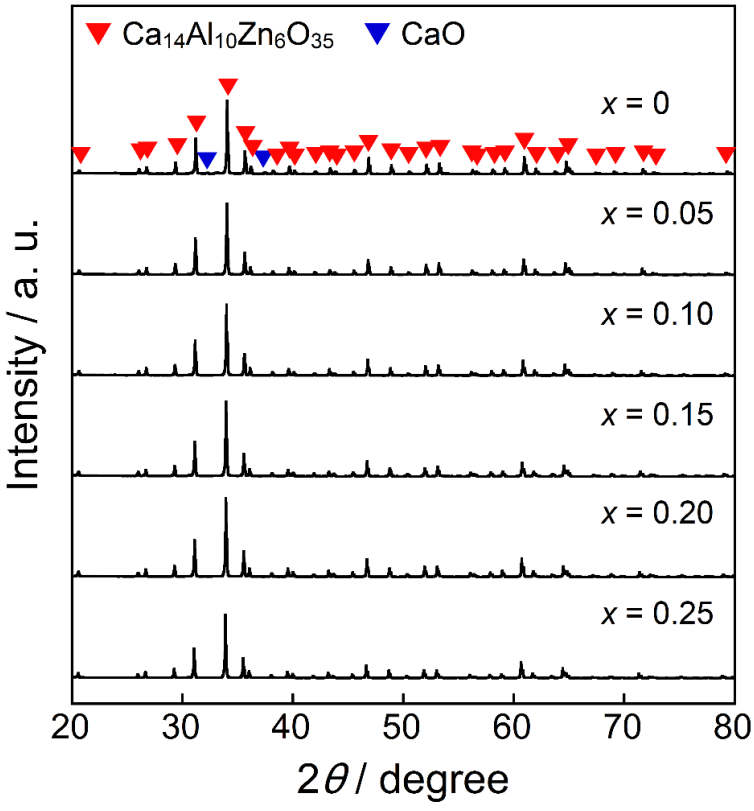

Figure 2.1 XRD patterns of the $Ca_{14}(Al_{1-x}Fe_x)_{10}Zn_6O_{35}$ ($0 \leq x \leq 0.25$) samples.

Table 2.2 Lattice volume of $Ca_{14}(Al_{1-x}Fe_x)_{10}Zn_6O_{35}$ ($0 \leq x \leq 0.25$)

x	Lattice volume / nm^3
0	3.2972(1)
0.05	3.3068(1)
0.10	3.3175(1)
0.15	3.3259(2)
0.20	3.3345(1)
0.25	3.3425(2)

2.3.3 Field-emission-type scanning electron microscopic (FE-SEM) image

Figure 2.2 shows the FE-SEM images of the $Ca_{14}(Al_{1-x}Fe_x)_{10}Zn_6O_{35}$ ($0 \leq x \leq 0.25$) samples. Coarse particles having diameters in the range of 20–30 μm were observed in all samples.

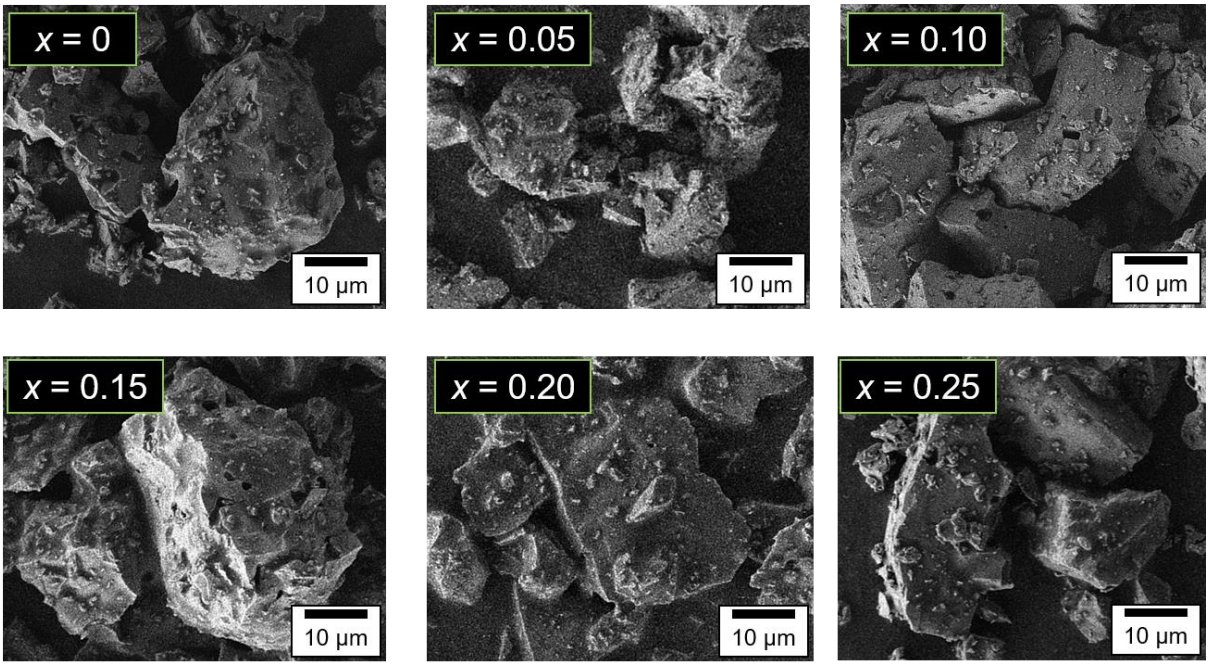

Figure 2.2 FE-SEM images of the $Ca_{14}(Al_{1-x}Fe_x)_{10}Zn_6O_{35}$ ($0 \leq x \leq 0.25$) samples.

2.3.4 Reflectance spectra

The UV–Vis diffuse reflectance spectra of the $Ca_{14}(Al_{1-x}Fe_x)_{10}Zn_6O_{35}$ ($0 \leq x \leq 0.25$) samples are depicted in **Figure 2.3**. High reflectance was observed in the visible light region for the non-doped $Ca_{14}Al_{10}Zn_6O_{35}$ ($x = 0$) sample. The optical absorption corresponding to the O_{2p}–Zn_{3d} charge transfer transition was observed at a wavelength of 380 nm and shorter.[72] In the case of the Fe^{3+}-doped $Ca_{14}(Al_{1-x}Fe_x)_{10}Zn_6O_{35}$ ($0.05 \leq x \leq 0.25$) samples, on the other hand, strong absorption bands due to the O_{2p}–Fe_{3d} charge transfer transition were observed in the same wavelength region as well as the d–d transition of Fe^{3+} in the range of violet to green blue (380−490 nm). According to the Tanabe–Sugano diagram, the absorption band from 380 to 490 nm is assigned to the $^6A_1(^6S) \rightarrow {}^4E(^4D)$ transition of the Fe^{3+}.[62] In addition, the optical absorption around 600 nm, corresponding to the $^6A_1(^6S) \rightarrow {}^4T_2(^4G)$ transition of Fe^{3+},[62] also increased with increasing the Fe^{3+} concentration.

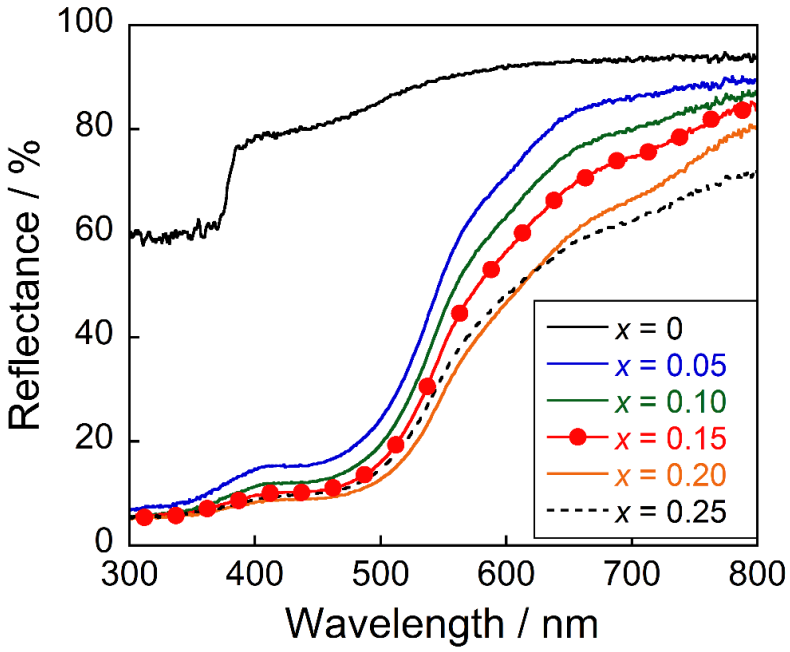

Figure 2.3 UV–Vis diffuse reflectance spectra of the $Ca_{14}(Al_{1-x}Fe_x)_{10}Zn_6O_{35}$ ($0 \leq x \leq 0.25$) samples.

2.3.5 Color properties

The *L*a*b*Ch°* color coordinate data for the $Ca_{14}(Al_{1-x}Fe_x)_{10}Zn_6O_{35}$ ($0 \leq x \leq 0.25$) pigments are summarized in **Table 2.3**. The photographs these pigments are also displayed in **Figure 2.4**. It is obvious that both the *a** and *b** values increased in a positive direction, by the introduction of Fe^{3+} in the host $Ca_{14}Al_{10}Zn_6O_{35}$ lattice.

Table 2.3 *L*a*b*Ch°* color coordinate data for the $Ca_{14}(Al_{1-x}Fe_x)_{10}Zn_6O_{35}$ ($0 \leq x \leq 0.25$) pigments

x	*L**	*a**	*b**	*C*	*h°*
0	94.4	−1.03	+6.07	6.16	99.6
0.05	79.1	+8.46	+58.4	59.0	81.8
0.10	74.8	+11.7	+59.0	60.1	78.8
0.15	67.9	+14.6	+57.0	58.8	75.6
0.20	67.0	+13.6	+52.0	53.7	75.3
0.25	65.5	+12.2	+52.0	53.4	76.8

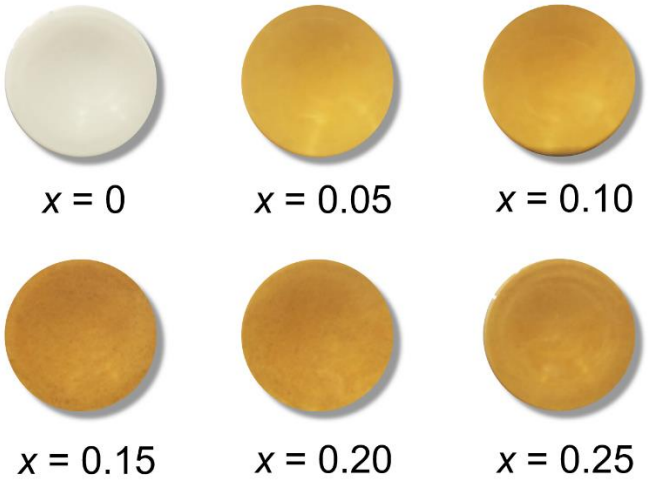

Figure 2.4 Photographs of the $Ca_{14}(Al_{1-x}Fe_x)_{10}Zn_6O_{35}$ ($0 \leq x \leq 0.25$) pigments.

As the optical absorption due to the $^6A_1(^6S) \rightarrow {}^4T_2(^4G)$ transition of Fe^{3+} appeared more intensely with increasing the Fe^{3+} concentration, the reflection of the yellow light decreased. As a result, the color of the samples gradually became reddish with increasing the Fe^{3+} content and it changed from yellow to orange. Since the samples in which the Fe^{3+} content was 20 mol% and above showed low reflectance in the orange light region, their C values decreased. The $h°$ values of the Fe^{3+}-doped $Ca_{14}(Al_{1-x}Fe_x)_{10}Zn_6O_{35}$ ($0.05 \leq x \leq 0.25$) pigments are fallen within the yellow–orange region (35°–70° for orange, 70°–105° for yellow). Furthermore, their values reduced as the amount of Fe^{3+} increased. The $h°$ values of the $Ca_{14}(Al_{0.85}Fe_{0.15})_{10}Zn_6O_{35}$ and $Ca_{14}(Al_{0.80}Fe_{0.20})_{10}Zn_6O_{35}$ pigments were almost same and were the smallest among the $Ca_{14}(Al_{1-x}Fe_x)_{10}Zn_6O_{35}$ ($0.05 \leq x \leq 0.25$) pigments. These results indicate that the color of those pigments is the most orangish, but the C value of $Ca_{14}(Al_{0.85}Fe_{0.15})_{10}Zn_6O_{35}$ was larger than

that of $Ca_{14}(Al_{0.80}Fe_{0.20})_{10}Zn_6O_{35}$. Accordingly, $Ca_{14}(Al_{0.85}Fe_{0.15})_{10}Zn_6O_{35}$ showed the most intense orange color among the $Ca_{14}(Al_{1-x}Fe_x)_{10}Zn_6O_{35}$ samples synthesized in this study.

2.3.6 Chemical and thermal stability tests

The chemical and thermal stabilities of the $Ca_{14}(Al_{0.85}Fe_{0.15})_{10}Zn_6O_{35}$ pigment were evaluated using the powder sample, and the results were compared with those of the commercially available Bayferrox® 960 (Fe_2O_3–FeOOH, Ozeki Co. Ltd.). The acid/base resistance of these pigments was tested in 4% acetic acid and 4% ammonium bicarbonate solutions, and these pigments were dispersed into the acid/base solutions. After leaving them at room temperature for 24 h, the samples were washed with deionized water and ethanol, and then dried at room temperature. To evaluate the thermal stability, $Ca_{14}(Al_{0.85}Fe_{0.15})_{10}Zn_6O_{35}$ and Bayferrox® 960 were heated in an aluminum silicate (mullite) crucible at 700 °C for 5 h under an air atmosphere and cooled to room temperature. The color of the pigment after the chemical and thermal stability tests was evaluated using the colorimeter. The *L*a*b*Ch*° color coordinate data are summarized in **Table 2.4**. The color of the present $Ca_{14}(Al_{0.85}Fe_{0.15})_{10}Zn_6O_{35}$ pigment was almost unchanged in the basic ammonium bicarbonate solution, but unfortunately, the color degradation was observed by soaking it in the acetic acid solution. On the other hand, Bayferrox® 960 has enough chemical stability.

Table 2.4 *L*a*b*Ch°* color coordinate data for $Ca_{14}(Al_{0.85}Fe_{0.15})_{10}Zn_6O_{35}$ and Bayferrox® 960 (Fe_2O_3–FeOOH) before and after chemical and thermal stability tests

$Ca_{14}(Al_{0.85}Fe_{0.15})_{10}Zn_6O_{35}$					
Treatment	*L**	*a**	*b**	*C*	*h°*
None	67.9	+14.6	+57.0	58.8	75.6
CH_3COOH	67.1	+11.7	+35.6	37.5	71.8
NH_4HCO_3	62.4	+19.8	+58.9	62.1	71.4
700 °C in air	67.7	+15.4	+58.4	60.1	75.2
Bayferrox® 960 (Fe_2O_3–FeOOH)					
Treatment	*L**	*a**	*b**	*C*	*h°*
None	59.1	+21.0	+47.5	51.9	66.1
CH_3COOH	57.0	+21.7	+47.1	51.6	65.3
NH_4HCO_3	56.2	+21.8	+47.1	51.9	65.2
700 °C in air	43.0	+33.2	+37.2	49.9	48.3

Figure 2.5 shows the XRD patterns of $Ca_{14}(Al_{0.85}Fe_{0.15})_{10}Zn_6O_{35}$ and Bayferrox® 960 before and after the heat resistance test. The $Ca_{14}(Al_{0.85}Fe_{0.15})_{10}Zn_6O_{35}$ pigment maintained a single-phase form without any impurity formation after the heat treatment. As shown in **Table 2.4**, the color was almost unchanged after the thermal stability test. In contrast, Bayferrox® 960 was oxidized after heating in air. The XRD pattern of Bayferrox® 960 heated at 700°C in air was in good agreement with that of a single-phase of Fe_2O_3 and no diffraction peaks corresponding to FeOOH were observed, indicating that FeOOH in Bayferrox® 960 was completely oxidized. After the heat treatment, the color of Bayferrox® 960 changed from orange to red, and this color degradation was caused by the oxidation of FeOOH to Fe_2O_3. From these results, it was confirmed that the $Ca_{14}(Al_{0.85}Fe_{0.15})_{10}Zn_6O_{35}$ pigment has high thermal stability.

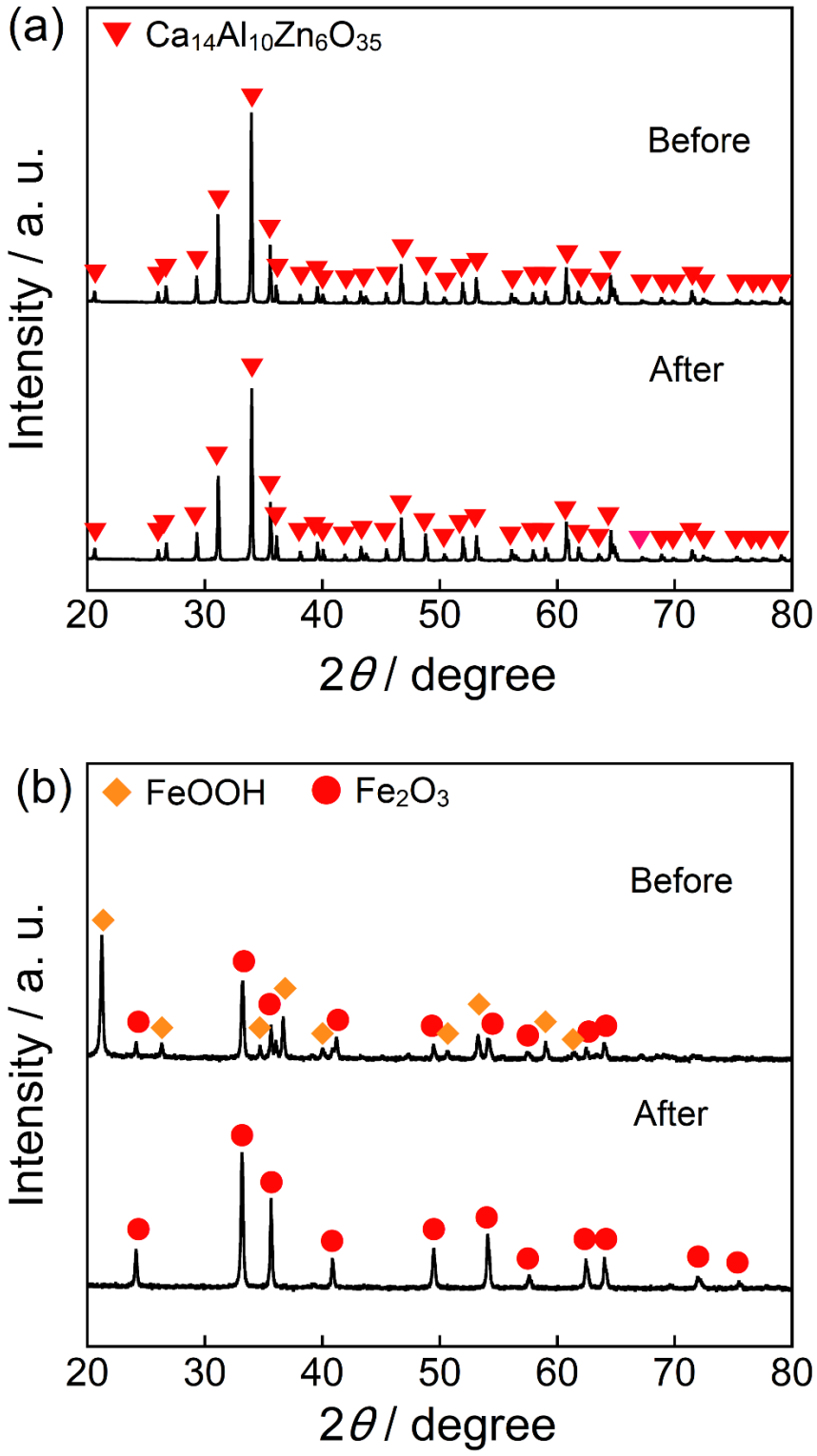

Figure 2.5 XRD patterns of $Ca_{14}(Al_{0.85}Fe_{0.15})_{10}Zn_6O_{35}$ (a) and Bayferrox® 960 [Fe_2O_3–FeOOH] (b) before and after the heat resistance test.

2.4 Conclusion

Novel and environmentally friendly inorganic orange pigments based on $Ca_{14}(Al_{1-x}Fe_x)_{10}Zn_6O_{35}$ ($0 \leq x \leq 0.30$) were synthesized by a conventional solid-state reaction. The Fe^{3+}-doped samples ($0.05 \leq x \leq 0.25$) strongly absorbed the visible light at wavelengths from 380 to 490 nm due to the d–d ($^6A_1 \rightarrow {}^4E$) transition of Fe^{3+}. In addition, the optical absorption around 600 nm, corresponding to the $^6A_1 \rightarrow {}^4T_2$ transition of Fe^{3+}, also increased with increasing the Fe^{3+} concentration. The sample color gradually turned from yellow to orange as the Fe^{3+} content increased. The most vivid orange color was obtained for the $Ca_{14}(Al_{0.85}Fe_{0.15})_{10}Zn_6O_{35}$ pigment. In addition, the thermal stability of this pigment was higher than that of commercially available Bayferrox® 960 pigment. Since the present pigment consists of only non-toxic elements, it is expected to be an environmentally friendly inorganic orange pigment.

Chapter 3

Synthesis and Color Evaluation of Ta^{5+}-Doped Bi_2O_3

3.1 Introduction

The novel inorganic orange pigments based on $Ca_{14}Al_{10}Zn_6O_{35}$ were described in previous Chapter 2. In this chapter, bismuth sesquioxide (Bi_2O_3) was focused on as a new base material of inorganic pigments. This compound has been confirmed as virtually nontoxic in medical references.[73–75] Bi_2O_3 has several polymorphs, such as α-phase (monoclinic structure), β-phase (tetragonal structure), γ-phase (body-centered cubic structure), and δ-phase (cubic fluorite structure).[76] The band structure of Bi_2O_3 is constituted by a valence band composed of a hybrid Bi_{6s} and O_{2p} orbital and a conduction band of Bi_{6p}.[77–81] A pale yellowish α phase stably exists at room temperature and is stable up to 730 °C. At 730 °C and above, the α phase is transferred to the orange δ phase. δ-Bi_2O_3 has been suggested as a good electrolyte material for solid oxide fuel cells and gas sensors, because this compound is stable at high temperatures and exhibits high oxide ion conductivity.[76,82–86]

When δ-Bi_2O_3 is cooled from a high temperature, a phase transition to the β phase takes place at 650 °C. Also, the metastable γ-Bi_2O_3 is formed below 650 °C on cooling δ-Bi_2O_3. The structure of β-Bi_2O_3 is a fluorite-based structure, but 25% of the oxide anion is regularly deficient.[87] Although the β and δ phases are unstainable at room temperature, they can be stabilized at room temperature when other cations are introduced into the Bi^{3+} site to form solid

solutions. In fact, niobium- and tantalum-doped $(Bi_{1-x}M_x)_2O_{3+2x}$ (M = Nb or Ta) solid solutions adopt β phase and δ phase at room temperature, respectively, to exhibit high oxide anion conductivity.[82] Although Nb^{5+}-doped Bi_2O_3 has been reported as an inorganic reddish-yellow pigment,[13] there is no report on the color evaluation of Ta^{5+}-doped Bi_2O_3 as an inorganic pigment.

Therefore, Ta^{5+}-doped Bi_2O_3 solid solutions, $(Bi_{1-x}Ta_x)_2O_{3+2x}$ ($0 \leq x \leq 0.20$), were synthesized by a conventional solid-state reaction and their color properties were evaluated as environmentally friendly inorganic orange pigments.

3.2 Experimental Procedure

3.2.1 Materials and methods

The $(Bi_{1-x}Ta_x)_2O_{3+2x}$ ($0 \leq x \leq 0.20$) samples were synthesized using a conventional solid-state reaction technique. Stoichiometric amounts of Bi_2O_3 (Kishida Chemical Co., Ltd., 99.9%) and Ta_2O_5 (Wako Pure Chemical Industries, Ltd., 99.9%) were mixed in an agate mortar. The homogenous mixtures were calcined in an aluminum silicate (mullite) crucible at 800 °C for 6 h in air. Finally, the samples were ground in an agate mortar before characterization.

3.2.2 Characterization

The crystal structures were identified by X-ray powder diffraction (XRD, Rigaku Ultima IV) using Cu Kα radiation (40 kV, 40 mA). The sampling width and scan speed were 0.02 °

and 6.0 ° min^{-1}, respectively. The lattice parameters and volumes were calculated from the peak angles, which were refined using α-Al_2O_3 as a standard and using CellCalc Ver. 2.20 software. The sample compositions analyzed using X-ray fluorescence spectroscopy (Rigaku, ZSX Primus) were in good agreement with the nominal stoichiometric compositions of the starting mixtures. The morphology of the $(Bi_{1-x}Ta_x)_2O_{3+2x}$ (x = 0, 0.03, 0.04, and 0.20) particles was investigated by using field-emission-type scanning electron microscopy (FE-SEM; JEOL, JSM-6701F). The optical reflectance spectra were measured with an ultraviolet−visible (UV−Vis) spectrometer (Shimadzu, UV-2550) with barium sulfate as a reference. The band gap energies of the samples were calculated from the absorption edge of the absorbance spectrum represented by the Kubelka–Munk function,

$$f(R) = (1 - R)^2/2R$$

where R is reflectance.[88] The color property was evaluated in terms of the Commission Internationale de l' clairage $L^*a^*b^*Ch°$ system using a colorimeter (Konica-Minolta, CR-300). The L^* parameter indicates the brightness or darkness of a color on relation to a neutral gray scale, and the a^* (the red–green axis) and the b^* (the yellow–blue axis) parameters express the color qualitatively. Chroma parameter (C) represents the color saturation of the pigments

and is calculated according to the following formula: $C = [(a^*)^2 + (b^*)^2]^{1/2}$. The parameter $h°$ ranges from 0 to 360°, and is calculated with the formula, $h° = \tan^{-1}(b^*/a^*)$.

3.3 Results and Discussion

3.3.1 X-ray powder diffraction (XRD)

Figure 3.1 shows the XRD patterns of the $(Bi_{1-x}Ta_x)_2O_{3+2x}$ ($0 \leq x \leq 0.20$) samples. The XRD patterns of α-, β-, and δ-Bi_2O_3 from the inorganic crystal structure database are also shown in this figure as references. The crystal structure depended on the Ta content in $(Bi_{1-x}Ta_x)_2O_{3+2x}$ (x = 0, 0.03, 0.04, 0.20); the monoclinic α-Bi_2O_3 structure (x = 0), the tetragonal β-Bi_2O_3 structure (x = 0.03, 0.04), and the cubic δ-Bi_2O_3 structure (x = 0.20) were obtained in a single-phase form, respectively. However, a mixture of multiple phases was observed in the samples with x = 0.02 and 0.10 because the Ta concentration is near the boundary of the phase transition.

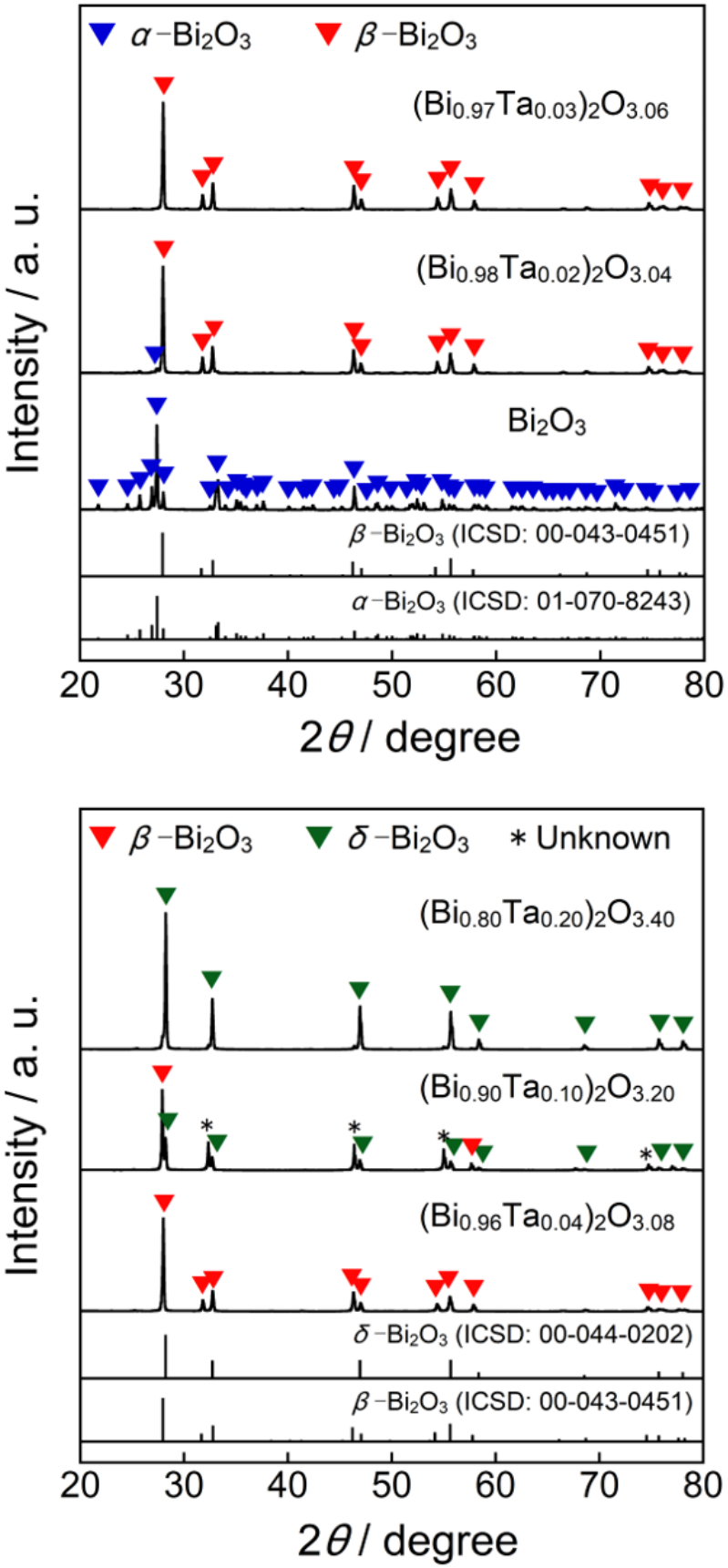

Figure 3.1 XRD patterns of the $(Bi_{1-x}Ta_x)_2O_{3+2x}$ ($0 \leq x \leq 0.20$) samples.

The lattice volumes of tetragonal $(Bi_{1-x}Ta_x)_2O_{2+x}$ (x = 0.03 and 0.04) and cubic $(Bi_{0.80}Ta_{0.20})_2O_{3.40}$ were calculated from the XRD angles, and the results are summarized in **Table 3.1**. The lattice volumes of the pure (Ta-free) tetragonal β-Bi_2O_3 and cubic δ-Bi_2O_3 are also listed as references,[89] where the numbers in parentheses indicate standard deviation. The cell volumes of the tetragonal $(Bi_{0.97}Ta_{0.03})_2O_{3.06}$ and the cubic $(Bi_{0.80}Ta_{0.20})_2O_{3.40}$ samples were smaller than those of the Ta-free tetragonal and cubic Bi_2O_3, respectively. The lattice volumes decreased with increasing the Ta^{5+} content, indicating that Bi^{3+} (ionic radius: 0.103 nm)[69] ions were partially substituted with Ta^{5+} (ionic radius: 0.064 nm)[69] ions. The cell volume of the tetragonal $(Bi_{0.96}Ta_{0.04})_2O_{3.08}$ sample was also smaller than that of the Ta-free tetragonal Bi_2O_3. However, the lattice volume of the tetragonal $(Bi_{0.96}Ta_{0.04})_2O_{3.08}$ and $(Bi_{0.97}Ta_{0.03})_2O_{3.06}$ samples was equal. These results indicate that the solubility limit of Ta^{5+} in the tetragonal β-phase was x = 0.03 for $(Bi_{1-x}Ta_x)_2O_{2+x}$.

Table 3.1 Lattice volumes of $(Bi_{1-x}Ta_x)_2O_{3+2x}$ (x = 0.03, 0.04, and 0.20) and Ta-free Bi_2O_3

Composition	Crystal system	Lattice volume / nm^3
$(Bi_{0.97}Ta_{0.03})_2O_{3.06}$	Tetragonal	0.33566(4)
$(Bi_{0.96}Ta_{0.04})_2O_{3.08}$	Tetragonal	0.33565(3)
Bi_2O_3[a]	Tetragonal	0.33754(3)
$(Bi_{0.97}Ta_{0.03})_2O_{3.06}$	Cubic	0.16402(1)
Bi_2O_3[a]	Cubic	0.18139(4)

[a] Cited from ref 89.

3.3.2 Field-emission-type scanning electron microscopic (FE-SEM) image

Figure 3.2 shows the FE-SEM images of the $(Bi_{1-x}Ta_x)_2O_{3+2x}$ (x = 0, 0.03, 0.04, and 0.20) samples obtained in a single-phase form. Although aggregated coarse particles were observed in all samples, it was found that only $(Bi_{0.80}Ta_{0.20})_2O_{3.40}$ was composed of small granular particles of about 1 μm somewhat thermally fused.

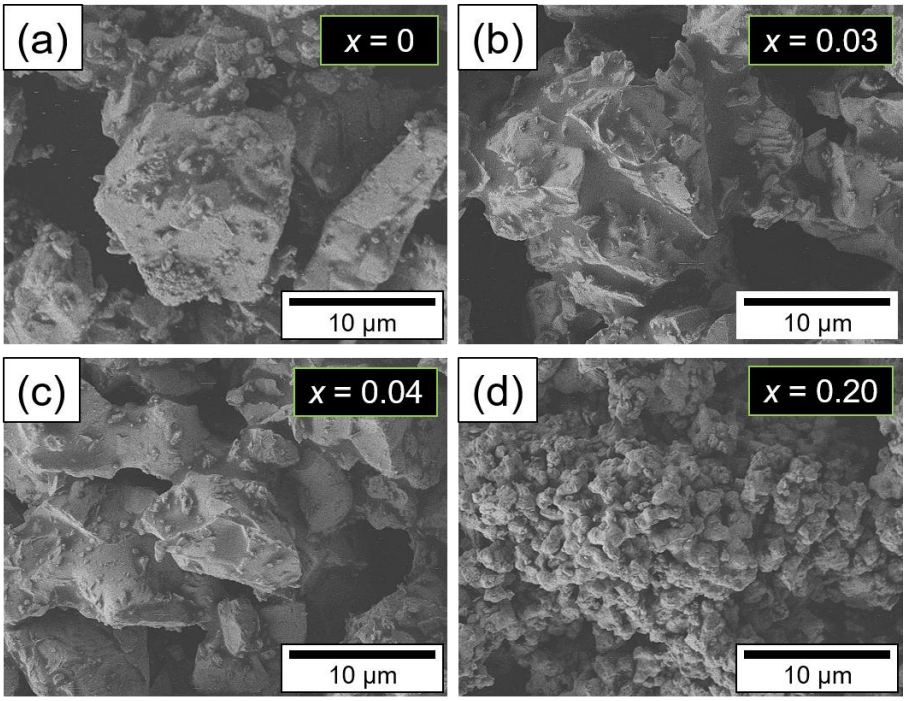

Figure 3.2 FE-SEM images of the synthesized Bi_2O_3 (a), $(Bi_{0.97}Ta_{0.03})_2O_{3.06}$ (b), $(Bi_{0.96}Ta_{0.04})_2O_{3.08}$ (c), and $(Bi_{0.80}Ta_{0.20})_2O_{3.40}$ (d).

3.3.3 Reflectance spectra

Figure 3.3 depicts the UV–Vis reflectance spectra of the $(Bi_{1-x}Ta_x)_2O_{3+2x}$ (x = 0, 0.03, 0.04 and 0.20) samples obtained in a single-phase form. In all samples, optical absorption was

observed by the energy transition from the valence band composed of the hybrid Bi_{6s} and O_{2p} orbitals to the conduction band composed of the Bi_{6p} orbital.[77–80] The tetragonal β-phase samples (x = 0.03 and 0.04) exhibited strong absorption at 480 nm or shorter, whereas the gradual spectral curve was observed for the cubic δ-phase sample (x = 0.20). The absorption wavelengths of the tetragonal $(Bi_{1-x}Ta_x)_2O_{3+2x}$ (x = 0.03 and 0.04) and cubic $(Bi_{0.80}Ta_{0.20})_2O_{3.40}$ samples were obviously observed on the longer wavelength side compared with the monoclinic Bi_2O_3 sample. This behavior was attributed to the fact that the band gap energy of the formers was smaller than that of the latter.

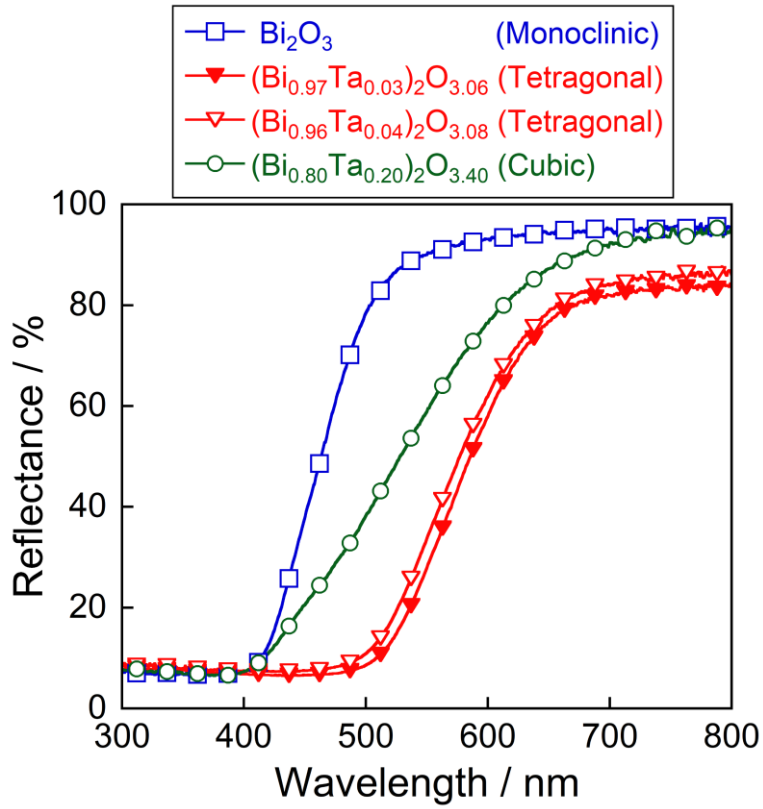

Figure 3.3 UV–Vis reflectance spectra of the $(Bi_{1-x}Ta_x)_2O_{3+2x}$ (x = 0, 0.03, 0.04, and 0.20) samples.

The average Bi–O bond distance in each $(Bi_{1-x}Ta_x)_2O_{3+2x}$ (x = 0, 0.03, and 0.20) sample, which was calculated with reference to the literature,[89,90] is summarized in **Table 3.2**, where the numbers in parentheses indicate the standard deviation. The average Bi–O bond length in the crystal lattice was short on the order of the tetragonal $(Bi_{0.97}Ta_{0.03})_2O_{3.06}$, the cubic $(Bi_{0.80}Ta_{0.20})_2O_{3.40}$, and the monoclinic Bi_2O_3 samples. Since the hybrid effect of the Bi_{6s} and O_{2p} orbitals in the valence band increases as the Bi–O bond distance decreases,[91,92] the width of the valence band also increases as the Bi–O bond distance becomes shorter. As a result, the band gap energy between the valence and the conduction bands decreases on decreasing the Bi–O bond distance.

Table 3.2 Average Bi−O bond distance in the $(Bi_{1-x}Ta_x)_2O_{3+2x}$ (x = 0, 0.03, and 0.20) samples

x	Crystal system	Average Bi–O bond distance / nm
0	Monoclinic	0.24636(3)
0.03	Tetragonal	0.23265(4)
0.20	Cubic	0.23703(4)

Accordingly, the band gap energy of each sample became small on the order of the tetragonal $(Bi_{0.97}Ta_{0.03})_2O_{3.06}$, the cubic $(Bi_{0.80}Ta_{0.20})_2O_{3.40}$, and the monoclinic Bi_2O_3 samples, corresponding to the short of the average bond length. Therefore, the optical absorption wavelength of the tetragonal $(Bi_{0.97}Ta_{0.03})_2O_{3.06}$ sample was located on the lowest energy (i.e., longer wavelength) side. The slope of the reflectance spectrum became moderate in the case of the cubic $(Bi_{0.80}Ta_{0.20})_2O_{3.40}$ sample, because of the reduction of the hybrid effect due to the

decrease in the Bi^{3+} content. Among the $(Bi_{1-x}Ta_x)_2O_{3+2x}$ samples synthesized in this study, the $(Bi_{0.97}Ta_{0.03})_2O_{3.06}$ sample exhibited the strongest absorption in the green-blue light region (480–490 nm), which is the complementary color of orange.

The UV–Vis reflectance spectrum of the $(Bi_{0.97}Ta_{0.03})_2O_{3.06}$ pigment was compared with those for the commercially available orange pigments such as Bayferrox® 960 and Bayferrox® 4960 (Fe_2O_3–FeOOH, Ozeki Co., Ltd.), as shown in **Figure 3.4**. The present $(Bi_{0.97}Ta_{0.03})_2O_{3.06}$ pigment showed higher reflectance in the wavelength region of 580–850 nm corresponding to the yellow–red light as compared with the commercially available orange pigments. But unfortunately, the reflectance in the green light region (520–570 nm) was also higher than those of the commercial ones.

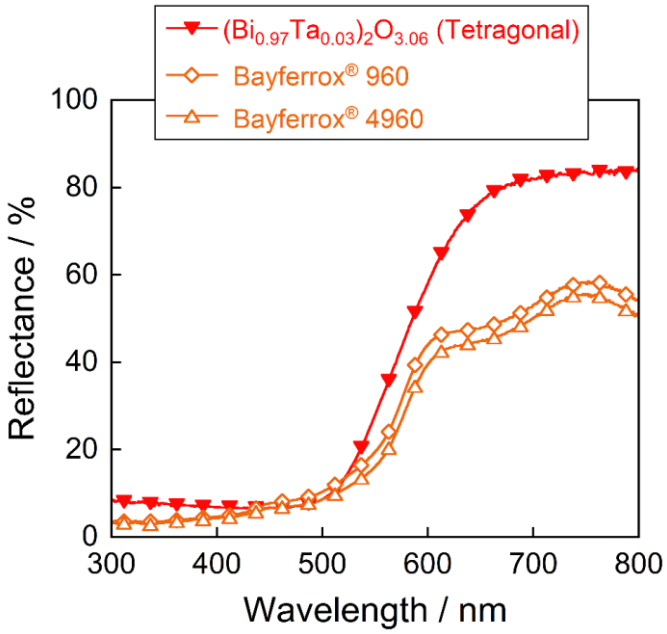

Figure 3.4 UV–Vis reflectance spectra for $(Bi_{0.97}Ta_{0.03})_2O_{3.06}$, Bayferrox® 960, and Bayferrox® 4960 pigments.

3.3.4 Color properties

The *L*a*b*Ch°* color coordinate data and band gap energies (E_g) for $(Bi_{1-x}Ta_x)_2O_{3+2x}$ (x = 0, 0.03, 0.04, and 0.20) and commercial orange Bayferrox® 960 and Bayferrox® 4960 pigments are summarized in **Table 3.3**. The photographs of these pigments are also displayed in **Figure 3.5**. It is obvious that both *a** and *b** values increased in a positive direction by the introduction of Ta^{5+} in the host Bi_2O_3 lattice. Among them, the tetragonal $(Bi_{0.97}Ta_{0.03})_2O_{3.06}$ sample strongly absorbed green and blue (complementary color of orange) lights and exhibited the most vivid orange color with the highest *a** value.

Table 3.3 *L*a*b*Ch°* color coordinate data and band gap energies (E_g) for $(Bi_{1-x}Ta_x)_2O_{3+2x}$ (x = 0, 0.03, 0.04, and 0.20), Bayferrox® 960, and Bayferrox® 4960 pigments

Samples	*L**	*a**	*b**	*C*	*h°*	E_g / eV
Bi_2O_3	94.0	−9.64	+31.5	32.9	107	2.85
$(Bi_{0.97}Ta_{0.03})_2O_{3.06}$	63.2	+17.3	+56.3	58.9	72.9	2.27
$(Bi_{0.96}Ta_{0.04})_2O_{3.08}$	66.1	+15.2	+60.6	62.5	75.9	2.29
$(Bi_{0.80}Ta_{0.20})_2O_{3.40}$	82.7	+4.70	+46.3	46.5	84.2	2.74
Bayferrox® 960	59.0	+21.0	+47.5	51.9	66.1	2.13
Bayferrox® 4960	55.9	+23.5	+47.3	52.8	63.6	2.12

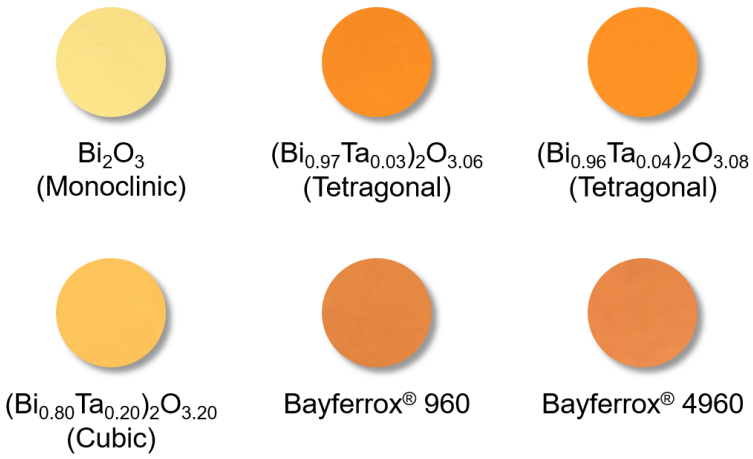

Figure 3.5 Photographs of the $(Bi_{1-x}Ta_x)_2O_{3+2x}$ (x = 0, 0.03, 0.04, and 0.20), Bayferrox® 960, and Bayferrox® 4960 pigments.

The color of materials can be affected by a combination of factors, such as particle size, packing density, crystal structure, and chemical composition. As the particle size of the pigment decreases, the color tends to be brighter or lighter.[93] As shown in **Figure 3.2**, there was no difference in the particle size of monoclinic Bi_2O_3 and tetragonal $(Bi_{1-x}Ta_x)_2O_{3+x}$ (x = 0.03 and 0.04). Therefore, the color of these pigments depends on the crystal system. In contrast, the particle size of $(Bi_{0.80}Ta_{0.20})_2O_{3.40}$ was smaller than those of other samples and the color of $(Bi_{0.80}Ta_{0.20})_2O_{3.40}$ was relatively light. The pale coloration can be attributed not only to the change of the crystal structure but also the reduction of the particle size.

As seen in **Table 3.3**, the redness value (a*) for the $(Bi_{0.97}Ta_{0.03})_2O_{3.06}$ pigment was slightly small compared to that of the commercial orange pigments. On the other hand, the yellowness value (b*) was larger than that of the commercially available orange pigments. As a result, it appeared yellowish orange.

3.3.5 Chemical stability test

The chemical stability of the $(Bi_{0.97}Ta_{0.03})_2O_{3.06}$ pigment was also evaluated. The powder sample was dispersed into 4% acetic acid and 4% ammonium bicarbonate aqueous solutions. After leaving them at room temperature for 6 h, the samples were washed with deionized water and ethanol and then dried at room temperature. The color of the samples after the chemical stability test was evaluated using the colorimeter. Unfortunately, slight color degradation was observed after the soaking test, as summarized in **Table 3.4**, so it is necessary to cover the surface using an inert substance such as silica to suppress the color degradation.

Table 3.4 *L*a*b*Ch°* color coordinates of $(Bi_{0.97}Ta_{0.03})_2O_{3.06}$ before and after the chemical stability test

Treatment	*L**	*a**	*b**	*C*	*h°*
Non-treatment	63.2	+17.3	+56.3	58.9	72.9
4% CH_3COOH	68.3	+13.8	+51.4	53.2	75.0
4% NH_4HCO_3	67.2	+14.6	+50.0	52.1	73.7

3.4 Conclusion

$(Bi_{1-x}Ta_x)_2O_{3+2x}$ ($0 \leq x \leq 0.20$) solid solutions were synthesized by a conventional solid-state reaction method. The crystal structure of the $(Bi_{1-x}Ta_x)_2O_{3+2x}$ (x = 0, 0.03, 0.04, 0.20) samples depended on the composition, and monoclinic α-phase (x = 0), tetragonal β-phase (x = 0.03, 0.04), and cubic δ-phase (x = 0.20) were obtained in a single-phase form. Among these samples, the $(Bi_{0.97}Ta_{0.03})_2O_{3.06}$ pigment strongly absorbed the green-blue light and the band

gap energy was 2.27 eV. This pigment presented a vivid yellowish orange color, because the redness value (a^*) of this pigment was slightly smaller and the yellowness value (b^*) was larger than those of commercial orange pigments. Although it is necessary to improve chemical stability, the $(Bi_{0.97}Ta_{0.03})_2O_{3.06}$ pigment has potential to be one of the environmentally friendly inorganic orange pigments.

Chapter 4

Effect of [MnO_6] Octahedra to the Coloring Mechanism of $(Li_{1-x}Na_x)_2MnO_3$

4.1 Introduction

A number of nontoxic red pigments have been developed by several researchers to replace the harmful pigments with the environment-friendly ones, as mentioned in Chapter 1. In this chapter, our research group focused on tetravalent manganese (Mn^{4+}) ion as a source of red color. Recently, Mn^{4+} has been investigated as an activator for the red-light emitting phosphors due to low cost and non-toxicity.[94–102] $K_2XF_6:Mn^{4+}$ (X = Si, Ge, Ti), $Li_2TiO_3:Mn^{4+}$, and $CaAl_{12}O_{19}:Mn^{4+}$ have been reported as examples of Mn^{4+}-doped phosphors.[100–102] These phosphors absorb the visible light in the wavelength ranges from 350 to 550 nm, which is attributed to the electronic transition between two 3d orbitals (t_{2g} and e_g) of Mn^{4+}. The optical absorption band due to the d–d transition is influenced by the crystal field around the Mn^{4+} ions. The Mn^{4+} content is controlled approximately by 1 mol % to avoid concentration quenching in phosphors. However, it is considered that the visible light in the region from 350 to 550 nm is strongly absorbed by further increasing the Mn^{4+} concentration and coloring of the sample can be recognized. Since the visible light around 550 nm corresponds to green light, it is expected that a reddish color, which is a complementary color of green, will be obtained.

For these reasons, Mn^{4+} is a promising coloring source to develop environment-friendly inorganic red pigments.

Lithium manganese oxide (Li_2MnO_3) was selected as a host material, and the components are nontoxic elements. It has been reported that the color of this material is brick-red or orange-red due to the optical absorption in the wavelength range between 350 and 550 nm, corresponding to the d–d transition of Mn^{4+} ions.[103,104] However, the red color purity of pure Li_2MnO_3 is not enough, and it is necessary to enhance the red color purity to make it a red pigment. Because the d–d transitions in transition metal cations are strongly influenced by the crystal field around them, the control of the optical absorption due to the d–d transition is possible by adjusting the crystal field energy. The d–d transition band shifts to the lower energy (i.e., longer wavelength) side, when the crystal field around the chromophore ions becomes weak due to the introduction of larger cations into the host material. Therefore, a more reddish color than that of pure Li_2MnO_3 will be obtained by doping larger cations. To enhance the red color purity of Li_2MnO_3, our research group selected Na^+ (ionic radius: 0.116 nm)[69] as a dopant because this is a nontoxic element and has the same valence with Li^+ (ionic radius: 0.090 nm).[69] Namely, Na^+-doped Li_2MnO_3 samples, $(Li_{1-x}Na_x)_2MnO_3$ ($0 \leq x \leq 0.10$), were synthesized by a solid-state reaction technique and the influences of differences in the geometric structure around the Mn^{4+} ions on the color properties were investigated.

4.2 Experimental Procedure

4.2.1 Materials and methods

The $(Li_{1-x}Na_x)_2MnO_3$ ($0 \leq x \leq 0.10$) samples were synthesized by a conventional solid-state reaction technique. Stoichiometric amounts of Li_2CO_3, MnO_2, and Na_2CO_3 were mixed with 5 cm^3 of ethanol in an agate mortar to obtain 1 g of the final product. The mixtures were heated in an alumina crucible at 1050 °C for 6 h in the atmosphere. Before characterization, the sample was ground in an agate mortar.

4.2.2 Characterization

The crystal structure of the samples was identified by X-ray powder diffraction (XRD; Rigaku, Ultima IV) with Cu-Kα radiation (40 kV and 40 mA). The data were collected by scanning over in the 2θ range of 20–80°, and the sampling width was 0.02°. The lattice volumes of the samples were calculated from the diffraction angles, which were refined using α-alumina as a standard and CellCalc Ver. 2.20 software. Rietveld refinement of the resulting XRD patterns in the 2θ range of 10−120° was performed by the RIETAN-FP software package to determine the precise crystal structure and investigate the coordination environment around Mn^{4+} ions for the $(Li_{1-x}Na_x)_2MnO_3$ (x = 0 and 0.07) samples.[105] From the Rietveld refinement, the following final R-factors were obtained: weighted pattern R-factor (R_{wp}), pattern R-factor (R_p), R-expected factor (R_e), R-structure factor (R_F), and goodness-of-fit indicator (S).

The particle size and morphology of the Li_2MnO_3 and $(Li_{0.93}Na_{0.07})_2MnO_3$ samples were observed with a field-emission-scanning electron microscope (FE-SEM; JEOL, JSM-6701F). The optical reflectance spectra were measured using an ultraviolet–visible–near-infrared (UV–Vis–NIR) spectrometer (JASCO, V-770) with a standard white plate as a reference. The chromatic properties of the samples were estimated in terms of the Commission Internationale de l' clairage (CIE) $L^*a^*b^*h°$ system using a colorimeter (Konica-Minolta, CR-300). The L^* parameter expresses the brightness or darkness of a color based on neutral grayscale, and the a^* (the red–green axis) and b^* (the yellow–blue axis) parameters indicate the color quantitatively. The value of $h°$ (hue angle) ranges from 0 to 360° and is calculated with the formula, $h° = \tan^{-1}(b^*/a^*)$. When $h°$ is in the region of $0 \leq h° \leq 35$, the color of the sample is red.

4.3 Results and Discussion

4.3.1 X-ray powder diffraction (XRD)

The XRD patterns of the synthesized $(Li_{1-x}Na_x)_2MnO_3$ ($0 \leq x \leq 0.10$) samples are shown in **Figure 4.1**. The XRD pattern of Li_2MnO_3 (No. 01-073-0152) from the inorganic crystal structure database (ICSD) is also depicted as a reference on the bottom. A single-phase Li_2MnO_3 structure was observed for all samples, and no diffraction peaks of other phases or impurities were detected in the patterns. The diffraction patterns of the samples corresponded

to that of the monoclinic Li_2MnO_3 from ICSD. The lattice volumes of the $(Li_{1-x}Na_x)_2MnO_3$ ($0 \leq x \leq 0.10$) samples were calculated from the diffraction angles in the XRD patterns. The compositional dependence of the lattice volume for the $(Li_{1-x}Na_x)_2MnO_3$ ($0 \leq x \leq 0.10$) solid solutions is shown in **Figure 4.2**. The cell volume increased with the increasing Na^+ concentration, which indicated that some Li^+ (ionic radius: 0.090 nm)[69] ions in the Li_2MnO_3 structure were substituted with larger Na^+ (ionic radius: 0.116 nm)[69] ones. These results indicate that the solid solutions of the monoclinic Li_2MnO_3 phase were successfully formed.

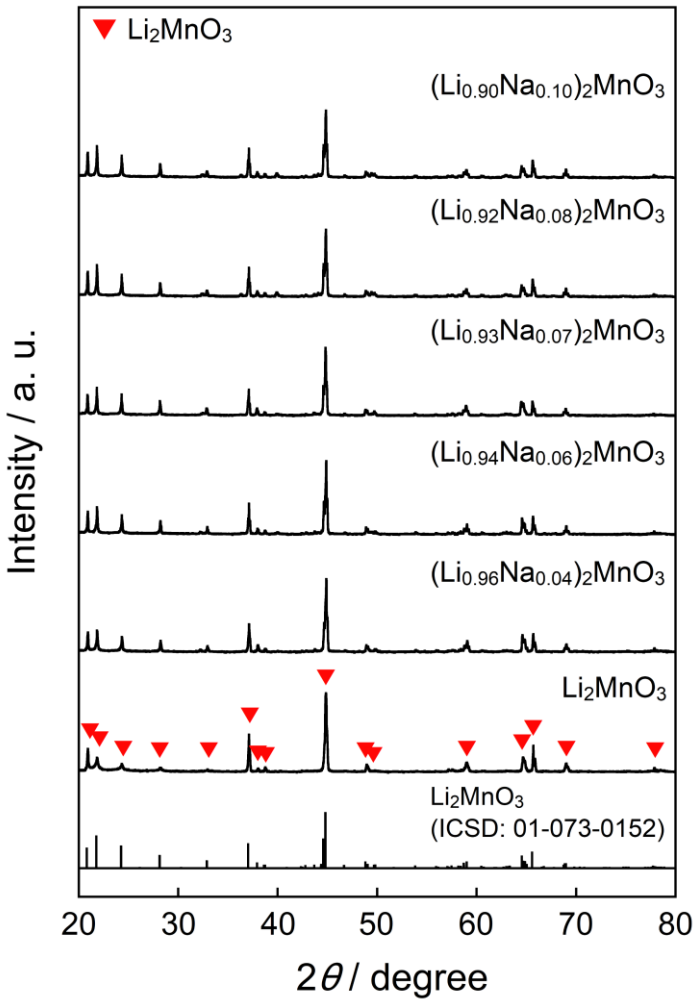

Figure 4.1 XRD patterns of the $(Li_{1-x}Na_x)_2MnO_3$ ($0 \leq x \leq 0.10$) samples.

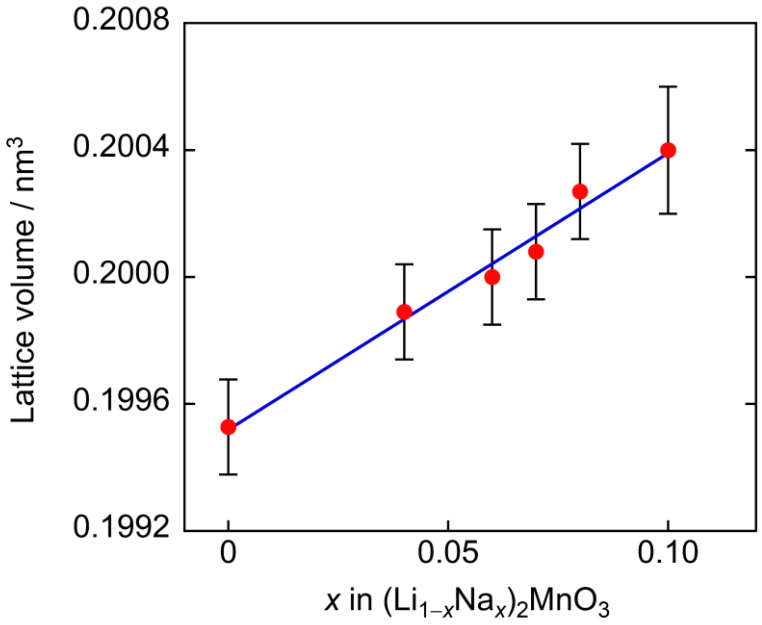

Figure 4.2 Composition dependence of the cell volume for the $(Li_{1-x}Na_x)_2MnO_3$ ($0 \leq x \leq 0.10$) samples.

4.3.2 Rietveld analysis

The crystal structure of Li_2MnO_3 has been investigated using the Rietveld method by many researchers.[106–111] Li_2MnO_3 has a layered rock-salt-type structure. It adopts a monoclinic unit cell with the *C*2/*m* (No. 12) space group. This layered structure is composed of Li^+ (2c and 4h sites) and Li^+/Mn^{4+} (2b and 4g sites) layers. These layers were alternately stacked via oxide anions. It has been reported by Boulineau et al. that Li^+ and Mn^{4+} ions in the Li^+/Mn^{4+} layer mainly occupy the 2b (Li-rich) and 4g (Mn-rich) sites, respectively, but the partial exchange between Li and Mn is possible on the 2b and 4g sites.[106]

The Rietveld structure refinement of the $(Li_{1-x}Na_x)_2MnO_3$ (x = 0 and 0.07) samples was carried out to investigate the geometric structure around the Mn^{4+} ions. **Figure 4.3** shows the Rietveld refinement profiles of the Li_2MnO_3 and $(Li_{0.93}Na_{0.07})_2MnO_3$ samples. The detailed crystallographic and structural parameters are tabulated in **Tables 4.1** and **4.2**, respectively. **Figure 4.4** displays the crystal structure of Li_2MnO_3 depicted by the VESTA program on the basis of the crystallographic parameters obtained from the Rietveld refinement.[112] As shown in **Figure 4.3**, the broadening of the peaks consisting of reflections was observed in the range from 2θ = 20 to 25°, corresponding to the [$\sqrt{3}a_{hex} \times \sqrt{3}a_{hex}$] superstructure caused by a Li(Na)/Mn ordering arrangement.[106] Therefore, the refinement was conducted in the 2θ ranges except in this region. The low R-factors were obtained for both $(Li_{1-x}Na_x)_2MnO_3$ (x = 0 and 0.07) samples. As shown in **Table 4.2**, almost all of the Na+ ions doped into the host lattice were located at the Li(1) site, and this result was in good agreement with the structure of $(Li_{0.95}Na_{0.05})_2MnO_3$ reported by Dong et al.[113]

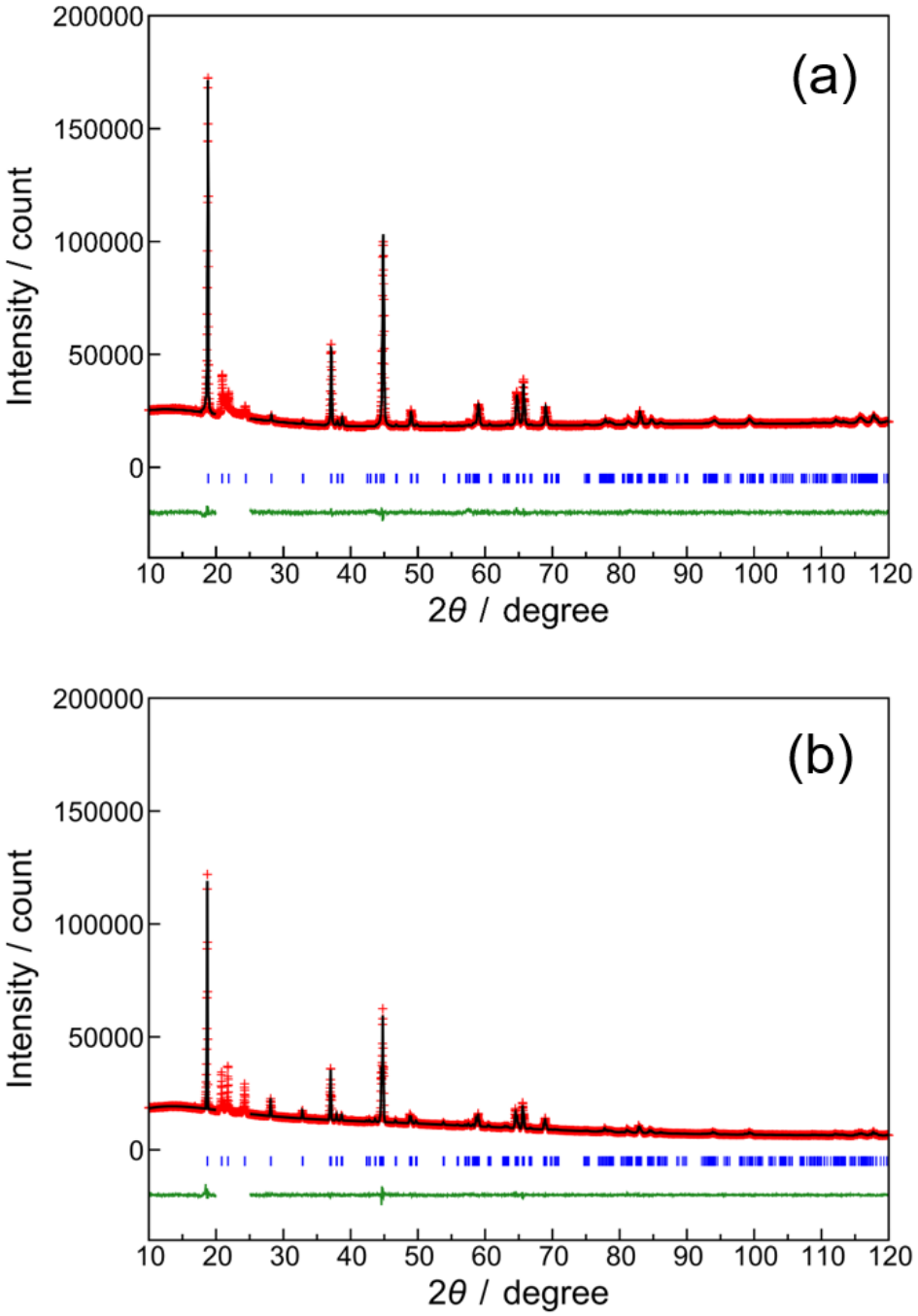

Figure 4.3 Observed intensities (red crossed symbol) and calculated patterns (solid black line) for the Rietveld structural refinement from the XRD data of Li_2MnO_3 (a) and $(Li_{0.93}Na_{0.07})_2MnO_3$ (b). The blue vertical bars represent the Bragg reflection peak positions. The bottom green line indicates the difference curve between the observed and the calculated patterns.

Table 4.1 Crystallographic parameters of $(Li_{1-x}Na_x)_2MnO_3$ (x = 0 and 0.07) obtained by Rietveld structural refinement analysis[a]

	$x = 0$	$x = 0.07$
Lattice parameter		
a / nm	0.49286(3)	0.493658(12)
b / nm	0.85311(3)	0.85404(2)
c / nm	0.50222(2)	0.503443(11)
β / °	109.236(4)	109.4020(14)
V / nm^3	0.19938(2)	0.200200(8)
***R*-factor**		
R_{wp}	1.275	1.683
R_p	0.873	1.061
R_e	0.694	0.958
S	1.837	1.757
R_F	5.265	5.668

[a] Crystal symmetry: monoclinic, space group: $C2/m$ (No. 12), number of formula units per unit cell: $Z = 4$.

Table 4.2 Structural parameters of the $(Li_{1-x}Na_x)_2MnO_3$ (x = 0 and 0.07) samples refined by the Rietveld method for the XRD patterns obtained at room temperature[a]

Li_2MnO_3							
Atom	Site	Occupancy (g)	Multiplicity × g	x	y	z	B_{iso} / Å^2
Li1	2b	0.618[b]	1.236	0	1/2	0	1.0
Mn1	2b	0.382(5)	0.764(10)	0	1/2	0	1.0
Li2	2c	1	2	0	0	1/2	1.0
Li3	4h	1	4	0	0.680(2)	1/2	1.0
Mn2	4g	0.809[b]	3.236	0	0.1642(4)	0	0.5
Li4	4g	0.191[b]	0.764	0	= y(Mn2)	0	0.5
O1	4i	1	4	0.215(2)	0	0.2247(13)	0.8
O2	8j	1	8	0.2471(14)	0.3197(6)	0.2188(7)	0.8
$(Li_{0.93}Na_{0.07})_2MnO_3$ (x = 0.07)							
Atom	Site	Occupancy (g)	Multiplicity × g	x	y	z	B_{iso} / Å^2
Li1	2b	0.668[c]	1.336	0	1/2	0	1.0
Mn1	2b	0.063(5)	0.126(10)	0	1/2	0	1.0
Na1	2b	0.269[c]	0.538	0	1/2	0	1.0
Li2	2c	1	2	0	0	1/2	1.0
Li3	4h	0.994[c]	3.976	0	0.663(3)	1/2	1.0
Na2	4h	0.006(4)	0.024(16)	0	= y(Li3)	1/2	1.0
Mn2	4g	0.969[c]	3.876	0	0.1672(3)	0	0.5
Li4	4g	0.031[c]	0.124	0	= y(Mn2)	0	0.5
O1	4i	1	4	0.226(2)	0	0.2257(10)	0.8
O2	8j	1	8	0.2586(9)	0.3263(7)	0.2174(6)	0.8

[a] The values of the isotropic atomic displacement parameter (B_{iso}) of the lithium, manganese, and oxygen sites were fixed at 1.0, 0.5, and 0.8 Å^2, respectively, with reference to the literature.[106,107,111] [b] The occupancies (g) of 2b and 4g sites in Li_2MnO_3 were linearly constrained to be the stoichiometric composition; g(Li1) = 1 − g(Mn1), g(Li4) = 0.5 × g(Mn1), and g(Mn2) = 1 − g(Li4). [c] The occupancy factors of 2b, 4h, and 4g sites in $(Li_{0.93}Na_{0.07})_2MnO_3$ were also linearly constrained: g(Li1) = 0.72 − g(Mn1) + 2 × g(Na2), g(Li3) = 1 − g(Na2), g(Li4) = 0.5 × g(Mn1), g(Mn2) = 1 − g(Li4), and g(Na1) = 0.28 − 2 × g(Na2).

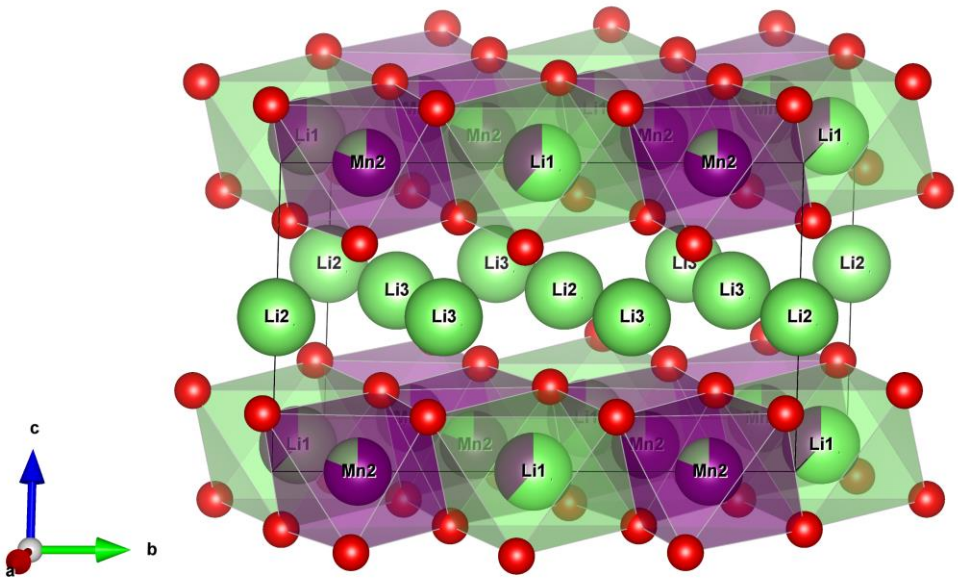

Figure 4.4 Crystal structure of Li_2MnO_3 (Li: green, Mn: violet, O: red) refined by the Rietveld method.

The average Mn(2)–O bond distance and distortion index (D) of the [Mn(2)O_6] octahedra in both $(Li_{1-x}Na_x)_2MnO_3$ (x = 0 and 0.07) samples are tabulated in **Table 4.3**. The numbers in parentheses indicate the standard deviation. A distortion index, D, based on bond lengths was calculated with the formula,[114)]

$$D = \frac{1}{6}\sum_{i=1}^{6}\frac{|l_i - l_{av}|}{l_{av}}$$

where l_i is the distance between the central atom and the ith coordinating atom and l_{av} indicates the average bond length. The average bond distance between Mn(2) and O increased as the Na^+ content increased. The increase in the D value indicates that the distortion of the octahedron

has become larger. For the [Mn(2)O_6]octahedra in the $(Li_{1-x}Na_x)_2MnO_3$ (x = 0 and 0.07) samples, the D value increased twofold by Na^+ doping, as shown in **Table 4.3**. These results indicate that the [Mn(2)O_6] octahedra were distorted by the introduction of Na^+ into the lattice.

Table 4.3 Average bond length of Mn(2)–O and distortion index (D) of the [Mn(2)O_6] octahedra in the refined $(Li_{1-x}Na_x)_2MnO_3$ (x = 0 and 0.07) structure

x	Average Mn(2)−O bond length / nm	D
0	0.1900(2)	0.0068
0.07	0.1911(2)	0.0154

4.3.3 Field-emission-type scanning electron microscopic (FE-SEM) image

Figure 4.5 shows the FE-SEM photographs of the Li_2MnO_3 and $(Li_{0.93}Na_{0.07})_2MnO_3$ samples. In the undoped Li_2MnO_3 (x = 0) sample, the primary particles aggregated and thermally fused to form the spherical secondary particles with lumpy surfaces. In contrast, the faceted primary particles, which had wide and flat surfaces, were observed for the $(Li_{0.93}Na_{0.07})_2MnO_3$ sample. In addition, the primary particle size for the sample with x = 0.07 was about 12 μm and almost equal to the secondary particle size of the undoped one.

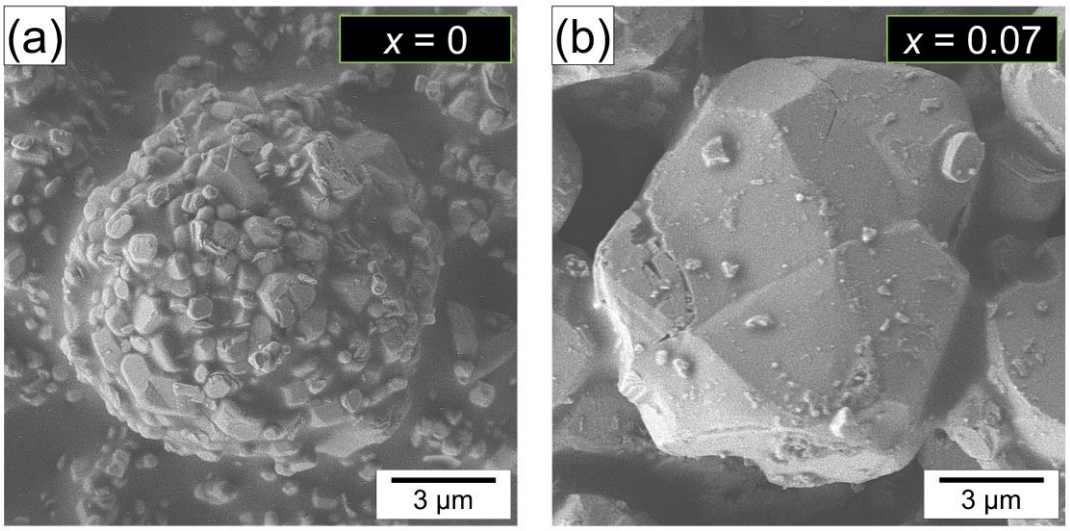

Figure 4.5 FE-SEM images of Li_2MnO_3 (a) and $(Li_{0.93}Na_{0.07})_2MnO_3$ (b).

4.3.4 Reflectance spectra

The ultraviolet–visible (UV–Vis) reflectance spectra for the $(Li_{1-x}Na_x)_2MnO_3$ ($0 \leq x \leq 0.10$) samples are shown in **Figure 4.6 (a)**. An enlarged view from 400 to 550 nm is also depicted in **Figure 4.6 (b)**. Optical absorption at the wavelength shorter than 550 nm was observed for all samples. The absorption band around 400 nm was attributed to the d–d transition of Mn^{4+}, which was assigned to the spin-allowed $^4A_{2g} \rightarrow {}^4T_{1g}$ transition, according to the Tanabe–Sugano diagram.[115] The absorption in the wavelength region between 400 and 550 nm corresponded to the spin-allowed $^4A_{2g} \rightarrow {}^4T_{2g}$ transition.[103] In addition to these optical absorptions, the absorption bands corresponding to the spin-forbidden $^4A_{2g} \rightarrow {}^2E_g$, $^2T_{1g}$ transitions were observed in the range of 650−710 nm.[103]

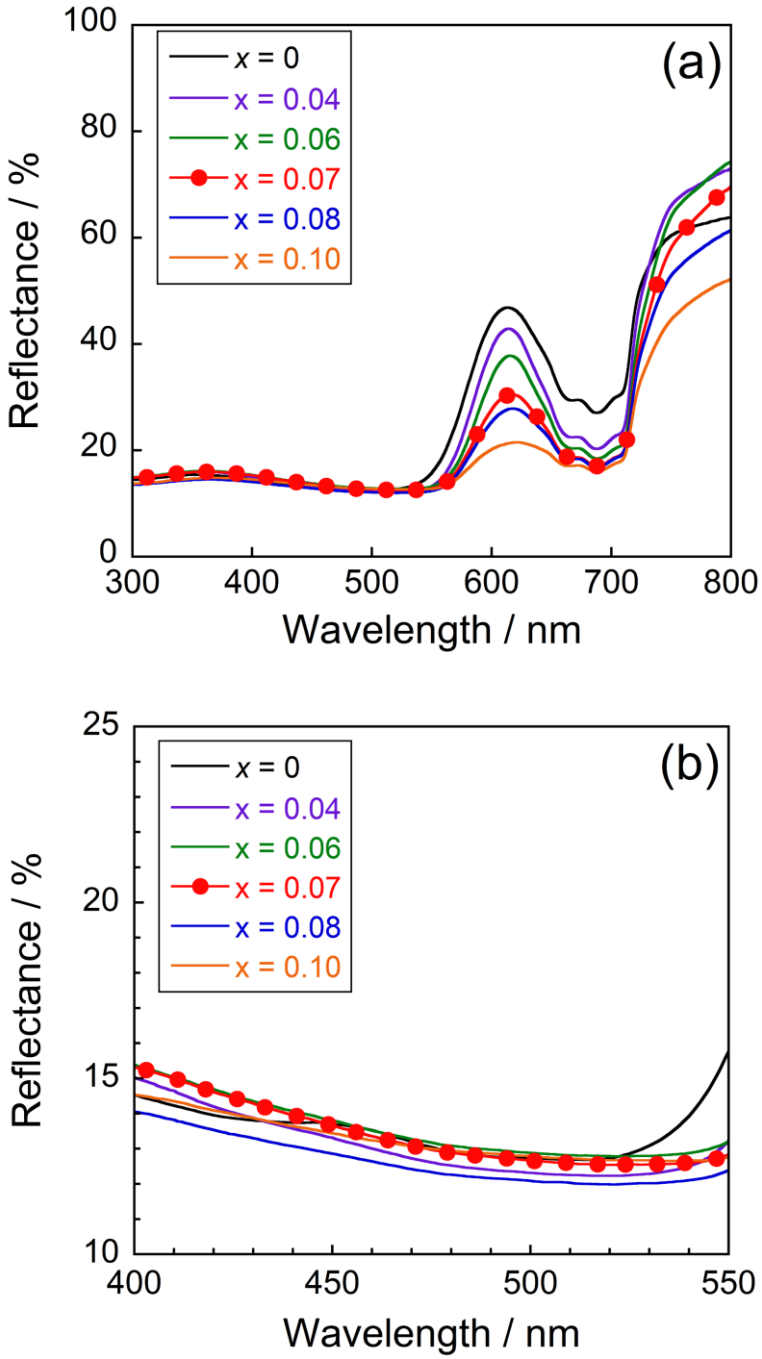

Figure 4.6 UV–Vis reflectance spectra (a) and enlarged spectra (b) of the $(Li_{1-x}Na_x)_2MnO_3$ ($0 \leq x \leq 0.10$) samples.

In the visible-light region from 400 to 700 nm, the light scattering capacity of a material tends to increase as the particle size decreases.[93] Accordingly, Li_2MnO_3 is expected to scatter

more visible light than $(Li_{0.93}Na_{0.07})_2MnO_3$ because the primary particle size of the former is smaller than that of the latter. Although such a result was obtained at wavelengths longer than 550 nm in the reflectance spectra, there was no significant change in the wavelength range from 400 to 550 nm, as shown in **Figure 4.6 (b)**. Therefore, the effect of the particle morphology on the optical properties is quite small, and the change in the reflectance is due to the difference in the coordination environment around the Mn^{4+} ion caused by the substitution of Li^+ with Na^+ in the lattice.

As seen in **Table 4.2**, in both of Li_2MnO_3 and $(Li_{0.93}Na_{0.07})_2MnO_3$, the amount (= multiplicity × *g*) of Mn(2) ions in the unit cells was significantly larger than that of Mn(1) ions. Therefore, the absorption wavelength of the spin-allowed $^4A_{2g} \rightarrow {}^4T_{2g}$ transition predominantly depended on the coordination environment at the Mn(2) site. The absorption band attributed to the $^4A_{2g} \rightarrow {}^4T_{2g}$ transition shifted to the longer wavelength side with Na^+ doping because the crystal field around the Mn^{4+} ion was weakened by the introduction of Na^+, which was larger than Li^+. In fact, the average Mn(2)–O bond distance for the Na^+-doped sample at $x = 0.07$ was longer than that for the undoped sample ($x = 0$), as shown in **Table 4.3**.

In contrast, the optical absorption bands corresponding to the spin-forbidden $^4A_{2g} \rightarrow {}^2E_g, {}^2T_{1g}$ transitions appeared more intensely with the increasing Na^+ content, but no peak shift was observed. As already explained for the results in **Table 4.3**, the $[Mn(2)O_6]$ octahedra in the lattice were more distorted when some Li^+ ions were substituted with Na^+ ions. Thus, the

$^4A_{2g} \rightarrow {}^2E_g, {}^2T_{1g}$ transitions were partially allowed because of the symmetry reduction caused by the enlargement of distortion. According to the Tanabe–Sugano diagram for d^3 electron configuration, the energy levels of ^2E_g and $^2T_{1g}$ are hardly affected by the crystal field strength. Therefore, the absorption intensity of the $^4A_{2g} \rightarrow {}^2E_g, {}^2T_{1g}$ transitions of Mn^{4+} increased due to the loss of symmetry, but the absorption wavelength hardly depended on the crystal field energy around the Mn^{4+} ion.

4.3.5 Color properties

The $L^*a^*b^*h°$ chromatic parameters for the $(Li_{1-x}Na_x)_2MnO_3$ ($0 \leq x \leq 0.10$) samples are summarized in **Table 4.4**. The sample photographs are also shown in **Figure 4.7**. The values of the brightness (L^*), redness (a^*), and yellowness (b^*) decreased as the concentration of Na^+ increased. These relationships were attributed to the differences in the absorption wavelengths and the intensities of the d–d transitions. As already discussed with respect to the results in **Figure 4.6**, the yellow–orange light (580–605 nm) was absorbed because the optical absorption band around 550 nm was shifted to the longer wavelength side by Na^+ doping. Additionally, the red-light reflection in the range from 605 to 700 nm was also reduced. As a result, all values of L^*, a^*, and b^* decreased. However, the hue angle ($h°$) became smaller by Na^+ doping and the color of the samples changed from orange to deep red. Among the $(Li_{1-x}Na_x)_2MnO_3$ ($0 \leq x \leq 0.10$) samples obtained in this work, $(Li_{0.93}Na_{0.07})_2MnO_3$ exhibited the lowest $h°$ value, and the sample was, namely, reddish in color.

Table 4.4 $L^*a^*b^*h^\circ$ Chromatic parameters for the $(Li_{1-x}Na_x)_2MnO_3$ ($0 \leq x \leq 0.10$) samples

x	L^*	a^*	b^*	h°
0	51.5	+30.8	+44.0	55.0
0.04	43.1	+30.7	+31.3	45.6
0.06	40.7	+25.3	+24.3	43.8
0.07	38.3	+24.8	+20.2	39.1
0.0	36.5	+23.3	+19.8	40.3
0.10	33.0	+22.1	+19.0	40.7

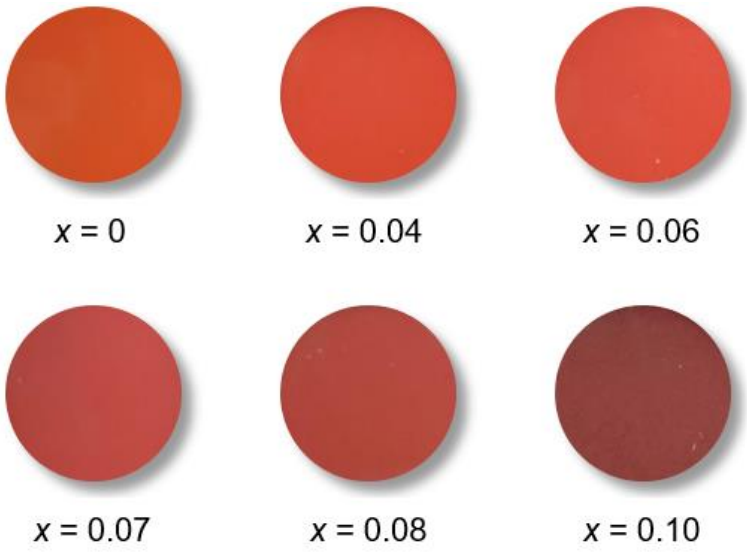

Figure 4.7 Photographs of the $(Li_{1-x}Na_x)_2MnO_3$ ($0 \leq x \leq 0.10$) samples.

4.3.6 Chemical stability and humidity resistance tests

The chemical stability and humidity resistance of $(Li_{0.93}Na_{0.07})_2MnO_3$ were also tested using a powder sample. To assess the chemical stability, the sample was soaked into 4% CH_3COOH and 4% NH_4HCO_3 aqueous solutions. After leaving them at room temperature for 3 h, the samples were washed with deionized water and ethanol. Finally, the samples were

dried at room temperature. The humidity resistance of the $(Li_{0.93}Na_{0.07})_2MnO_3$ sample was tested in a thermohygrostat at 90% relative humidity (RH) and 80 °C for 24 h. The sample color after the leaching and humidity resistance tests was evaluated with a calorimeter. Unfortunately, a slight color deterioration was observed after the leaching and humidity resistance tests, as summarized in **Table 4.5**. To suppress the color degradation, therefore, it is necessary to cover the surface using an inert substance such as silica.

Table 4.5 Color coordinates of $(Li_{0.93}Na_{0.07})_2MnO_3$ before and after the chemical stability and the humidity resistance tests

Treatment	*L**	*a**	*b**	*h*°
None	38.3	+24.8	+20.2	39.1
4% CH_3COOH	35.2	+21.8	+16.5	37.1
4% NH_4HCO_3	38.1	+23.2	+17.7	37.3
80 °C, 90%RH	35.2	+23.4	+18.7	38.6

4.3.7 Comparison with a conventional red pigment

The color parameters of the $(Li_{0.93}Na_{0.07})_2MnO_3$ pigment was compared to those for the commercially available cadmium red (Holbein works, Ltd., PG002) pigment, as summarized in **Table 4.6**. The photographs of these pigments are displayed in **Figure 4.8**. Unfortunately, the redness value of the $(Li_{0.93}Na_{0.07})_2MnO_3$ pigment was significantly lower than that of the commercial cadmium red one. On the other hand, the value of hue angle (*h*°) for the former

was even equal to that for the latter. This result indicated that the purity of red color for the $(Li_{0.93}Na_{0.07})_2MnO_3$ pigment was comparable to that for the commercial cadmium red pigment.

Table 4.6 Color coordinate data for the $(Li_{0.93}Na_{0.07})_2MnO_3$ and commercial cadmium red (CdS·CdSe) pigments

Pigment	*L**	*a**	*b**	*h*°
$(Li_{0.93}Na_{0.07})_2MnO_3$	38.3	+24.8	+20.2	39.1
CdS·CdSe	51.9	+63.7	+55.8	41.2

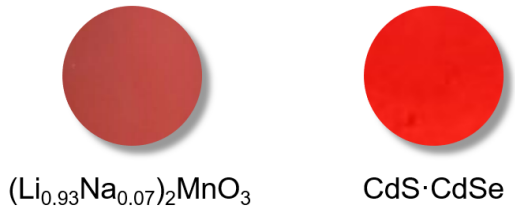

Figure 4.8 Photographs of the $(Li_{0.93}Na_{0.07})_2MnO_3$ and cadmium red (CdS·CdSe) pigments.

4.4 Conclusion

$(Li_{1-x}Na_x)_2MnO_3$ ($0 \leq x \leq 0.10$) samples were synthesized by a solid-state reaction process. The Rietveld analysis of the $(Li_{1-x}Na_x)_2MnO_3$ ($x = 0$ and 0.07) samples indicated that the average Mn(2)–O bond distance was increased, and the $[Mn(2)O_6]$ octahedra were distorted by doping Na^+ into the Li^+ site. The spin-allowed $^4A_{2g} \rightarrow {}^4T_{2g}$ transition observed at the wavelength shorter than 550 nm shifted to the longer wavelength side due to the decrease of the crystal field strength around Mn^{4+}. No shift was observed in the spin-forbidden $^4A_{2g} \rightarrow {}^2E_g$, $^2T_{1g}$ transitions around 680 nm, but the absorption intensities increased with the increase

in the distortion of the [Mn(2)O_6] octahedra. Consequently, the sample color gradually turned from orange to deep red with increasing Na^+ concentration. This study proposes that the coordination environment around Mn^{4+} is one of the important factors to develop environmentally friendly inorganic red pigments containing Mn^{4+}.

Chapter 5

Improvement of Near-Infrared (NIR) Reflectivity and Black Color Tone by Doping Zn^{2+} into the $Ca_2Mn_{0.85}Ti_{0.15}O_4$ Structure

5.1 Introduction

As mentioned in Chapter 1, development of inorganic black pigments with high NIR reflective properties have been desired. In our previous study, calcium manganese oxide ($CaMnO_3$, Ca_2MnO_4, $Ca_3Mn_2O_7$, and $Ca_4Mn_3O_{10}$) pigments were synthesized to determine whether these compounds could be candidates for novel NIR-reflective black pigments Among these complex oxides, Ca_2MnO_4 was found to be best and ideal as a black pigment with high NIR reflectivity. To enhance the NIR reflective properties of Ca_2MnO_4, furthermore, Ti^{4+} was introduced into the Mn^{4+} site; $Ca_2Mn_{1-x}Ti_xO_4$ ($0 \leq x \leq 0.40$) pigments were synthesized and characterized as novel inorganic NIR-reflective black pigments. In particular, the NIR solar reflectance value (R_{NIR}) of the $Ca_2Mn_{0.85}Ti_{0.15}O_4$ pigment was significantly higher than those of commercially available black pigments for thermal shielding.[59] But, unfortunately, this pigment exhibited slightly reddish black color.

Because of this situation, Zn^{2+} was doped into the Mn^{4+} site to improve the blackness of $Ca_2Mn_{0.85}Ti_{0.15}O_4$ without decreasing the NIR reflectance. The reasons for selecting Zn^{2+} as a dopant were that Zn^{2+} does not show optical absorption in the NIR region and the ionic radius

of Zn^{2+} (0.0740 nm)[69] is relatively close to that of Mn^{4+} (0.0530 nm)[69] in size. Therefore, $Ca_2Mn_{0.85-x}Ti_{0.15}Zn_xO_{4-x}$ ($0 \leq x \leq 0.10$) samples were synthesized, and the NIR reflectance and color properties were characterized. Finally, the Zn^{2+} concentration was optimized to meet both enough black hue and high NIR reflectivity.

5.2 Experimental Procedure

5.2.1 Materials and methods

The $Ca_2Mn_{0.85-x}Ti_{0.15}Zn_xO_{4-x}$ ($0 \leq x \leq 0.10$) samples were synthesized using a conventional solid-state reaction method. Stoichiometric amounts of $CaCO_3$ (FUJIFILM Wako Pure Chemical), MnO_2 (FUJIFILM Wako Pure Chemical), TiO_2 (FUJIFILM Wako Pure Chemical), and ZnO (Kishida Chemical) were mixed in an agate mortar. The mixtures were calcined in an alumina boat at 1200 °C for 6 h under an air atmosphere. Finally, the samples were ground in an agate mortar before characterization.

5.2.2 Characterization

The samples synthesized were characterized by X-ray powder diffraction (XRD; Rigaku, Ultima IV) with Cu-Ka radiation (40 kV and 40 mA). The sampling width and the scan speed were 0.02° and 6 min^{-1}, respectively. The sample compositions analyzed using X-ray fluorescence spectroscopy (XRF; Rigaku, ZSX Primus) were in good agreement with the stoichiometric compositions of the starting mixtures. The lattice parameters and volumes were

calculated from the XRD peak angles, which were refined using α-Al2O3 as a standard and using CellCalc Ver. 2.20 software. The morphology of the $Ca_2Mn_{0.85-x}Ti_{0.15}Zn_xO_{4-x}$ (x = 0 and 0.08) particles was investigated by using field-emission-type scanning electron microscopy (FE-SEM; JEOL, JSM-6701F). The size distribution and the average particle size were estimated by measuring the diameters of 200 particles from the FE-SEM photographs.

The optical reflectance spectra were measured with an ultraviolet–visible–near-infrared (UV–Vis–NIR) spectrometer (JASCO, V-770 with an integrating sphere attachment) with barium sulfate for the visible light region and poly-tetrafluoroethylene (PTFE) for the NIR region as references. The total (R_{Tot}, 300–2500 nm) and NIR (R_{NIR}, 700–2500 nm) solar reflectance was calculated in accordance with the American Society for Testing and Materials (ASTM) Standard G173-03, and was expressed as the integral of the product of the observed spectral reflectance and the solar irradiance divided by the integral of the solar irradiance, both integrated over the each range as in the formula

$$R_{\mathrm{Tot/NIR}} = \frac{\int_{\mathrm{Tot/NIR}}^{2500} r(\lambda) i(\lambda) \mathrm{d}\lambda}{\int_{\mathrm{Tot/NIR}}^{2500} i(\lambda) \mathrm{d}\lambda}$$

where $r(\lambda)$ is the spectral reflectance obtained from the experiment and $i(\lambda)$ is the standard solar spectrum (W m^{-2} nm^{-1}). The color property was evaluated in terms of the Commission Internationale de l′Eclairage (CIE) $L^*a^*b^*C$ system using a colorimeter (Konica-Minolta, CR-

300). The L^* parameter indicates the brightness or darkness of a color on relation to a neutral gray scale, and the a^* (the red–green axis) and the b^* (the yellow–blue axis) parameters express the color qualitatively. Chroma parameter (C) represents the color saturation of the pigments and is calculated according to the following formula: $C = [(a^*)^2 + (b^*)^2]^{1/2}$.

5.3 Results and Discussion

5.3.1 X-ray powder diffraction (XRD)

Figure 5.1 shows the XRD patterns of the $Ca_2Mn_{0.85-x}Ti_{0.15}ZnxO_{4-x}$ ($0 \leq x \leq 0.10$) samples. In the x range from 0 to 0.08, the target phase was obtained almost in a single-phase form, although nominal CaO and ZnO phases were detected. On the other hand, a small diffraction peak indexed to Ca_3ZnMnO_6 was observed at $2\theta = 32°$ as an additional impurity in the $Ca_2Mn_{0.75}Ti_{0.15}Zn_{0.10}O_{3.90}$ ($x = 0.10$) sample.

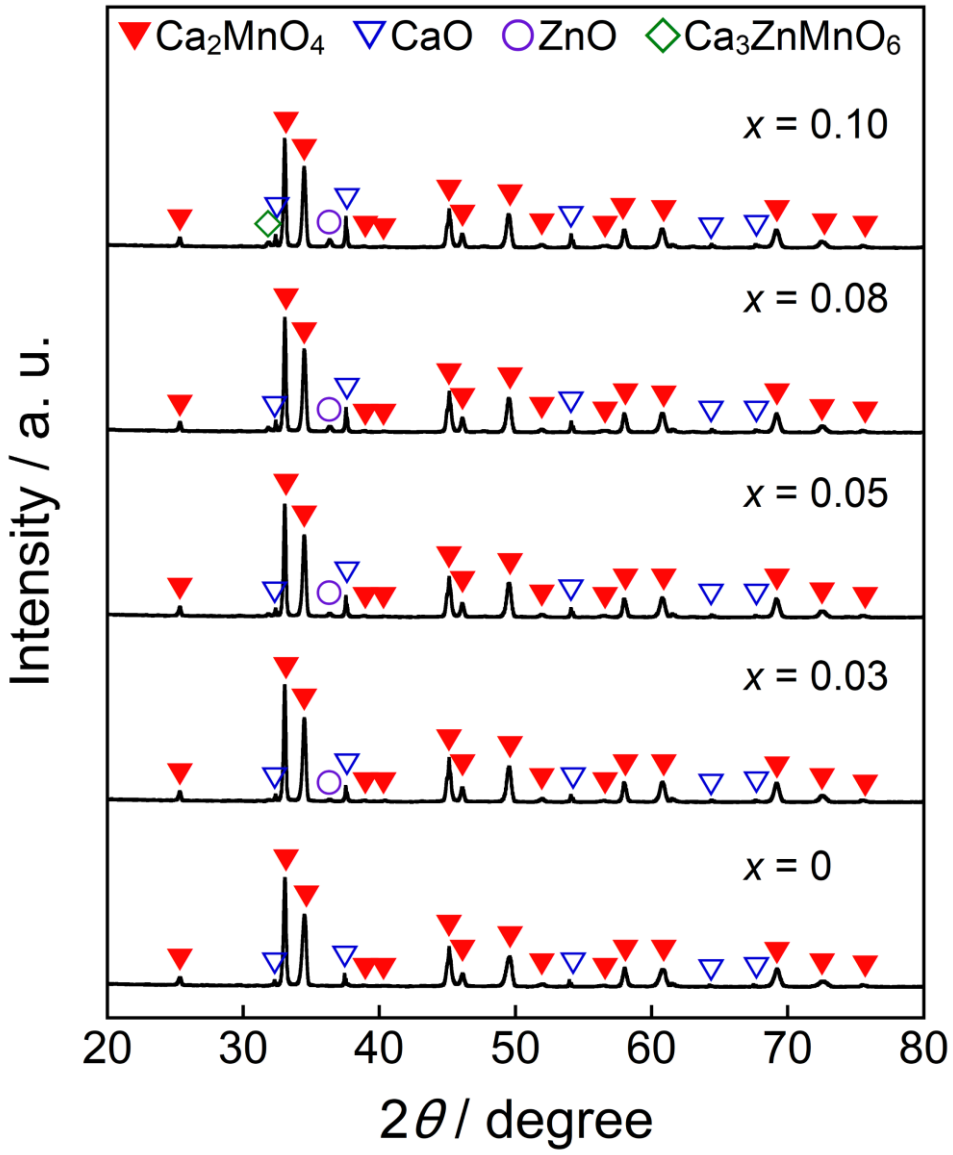

Figure 5.1 XRD patterns of the $Ca_2Mn_{0.85-x}Ti_{0.15}Zn_xO_{4-x}$ ($0 \leq x \leq 0.10$) samples.

Ca_2MnO_4 forms a tetragonal structure with space group of $I4_1/acd$ (No. 142). **Figure 5.2** shows the crystal structure of Ca_2MnO_4 illustrated using the VESTA program,[112] based on the crystallographic data reported by Leonowicz et al.[116] The [MnO_6] octahedra share corners with each other to form a two-dimensional perovskite-type array, and this [MnO_6] layer is interleaved by CaO layers in the c-axis direction. The Mn^{4+} ion in the [MnO_6] octahedron is

coordinated by two O^{2-}(1) ions in the *c*-axis direction and four O^{2-}(2) ions on the ab plane. The Mn–O(1) and Mn–O(2) bond distances are 0.1944 nm and 0.1856 nm, respectively.[116] Accordingly, the [MnO_6] octahedron is tetragonally distorted.

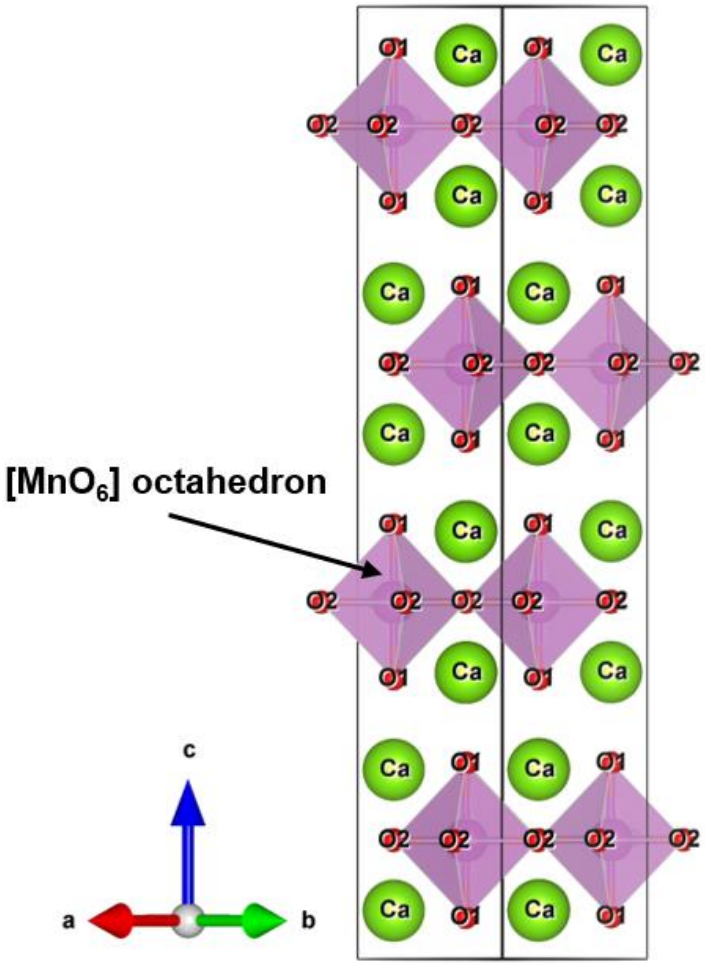

Figure 5.2 Crystal structure of Ca_2MnO_4.

The lattice parameters (*a*, *c*, and *V*) and the *c*/*a* ratios of all samples synthesized in this study were calculated from the XRD peak angles. These results are summarized in **Table 5.1**,

where the numbers in parentheses indicate standard deviations. The cell volume increased as the Zn^{2+} concentration increased in the range of $0 \leq x \leq 0.08$, indicating that some Mn^{4+} (ionic radius: 0.0530 nm)[69] ions were partially substituted with the larger Zn^{2+} (ionic radius: 0.0740 pm)[69] ions. However, the lattice volumes of $Ca_2Mn_{0.77}Ti_{0.15}Zn_{0.08}O_{3.92}$ (x = 0.08) and $Ca_2Mn_{0.75}Ti_{0.15}Zn_{0.10}O_{3.90}$ (x = 0.10) were equal. These results indicate that the solubility limit of Zn^{2+} was approximately x = 0.08 in $Ca_2Mn_{0.85-x}Ti_{0.15}Zn_xO_{4-x}$.

Table 5.1 Lattice parameters (a, c, and V) and c/a ratio of the $Ca_2Mn_{0.85-x}Ti_{0.15}Zn_xO_{4-x}$ ($0 \leq x \leq 0.10$) samples

x	a / nm	c / nm	c/a	V / nm^3
0	0.52084(7)	2.4121(4)	4.6312(10)	0.6543(2)
0.03	0.52091(12)	2.4140(9)	4.634(2)	0.6550(4)
0.05	0.52096(10)	2.4159(7)	4.637(2)	0.6557(3)
0.08	0.52110(12)	2.4167(8)	4.638(2)	0.6562(4)
0.10	0.5211(2)	2.4168(12)	4.638(3)	0.6562(6)

Considering the charge compensation, the electroneutrality will be maintained by the generation of either higher valence $Mn^{5+/7+}$ or the formation of oxide anion vacancies, when Zn^{2+} is doped into the Mn^{4+} site. However, Mn^{5+} is unstable in oxides and tends to transfer into more stable Mn^{4+} and Mn^{7+}.[117] When Mn^{7+} (ionic radius: 0.046 nm)[69] is generated in the structure for charge compensation, the lattice volume should increase nonlinearly, but that is not the case. Therefore, it is reasonable to consider that the electrical neutrality of $Ca_2Mn_{0.85-x}Ti_{0.15}Zn_xO_{4-x}$ is maintained by the production of oxide anion vacancies.

The lattice parameters *a* and *c* also increased with increasing the Zn^{2+} content. However, the increase rates of the former and the latter were different. The crystal structure of $Ca_2(Mn, Nb)O_4$ was investigated by Taguchi.[118] When the Nb^{5+} ions were introduced into the Mn^{4+} site in Ca_2MnO_4, the *c*/*a* ratio decreased with increasing the Nb^{5+} content, and the distortion of the $[MnO_6]$ octahedra was alleviated.[118] On the contrary, in the case of the $Ca_2Mn_{0.85-x}Ti_{0.15}Zn_xO_{4-x}$ ($0 \leq x \leq 0.10$) samples synthesized in this study, the c/a ratio increased with increasing the amount of Zn^{2+} in the range of $0 \leq x \leq 0.05$, as seen in **Table 5.1**. Therefore, the distortion of the $[MnO_6]$ octahedra was increased by the partial substitution of Mn^{4+} with Zn^{2+}.

5.3.2 Field-emission-type scanning electron microscopic (FE-SEM) image

Figure 5.3 shows the FE-SEM images and size distributions of the $Ca_2Mn_{0.85-x}Ti_{0.15}Zn_xO_{4-x}$ ($x = 0$ and 0.08) samples. The faceted particles were observed in both samples. These particles were thermally fused due to the high-calcination temperature at 1200 °C. In both samples, the average particle size was 0.97 μm and there was no significant change in particle size, size distribution, and morphology. These results indicate that the changes in the optical and color properties of both samples were caused by the Zn^{2+} doping.

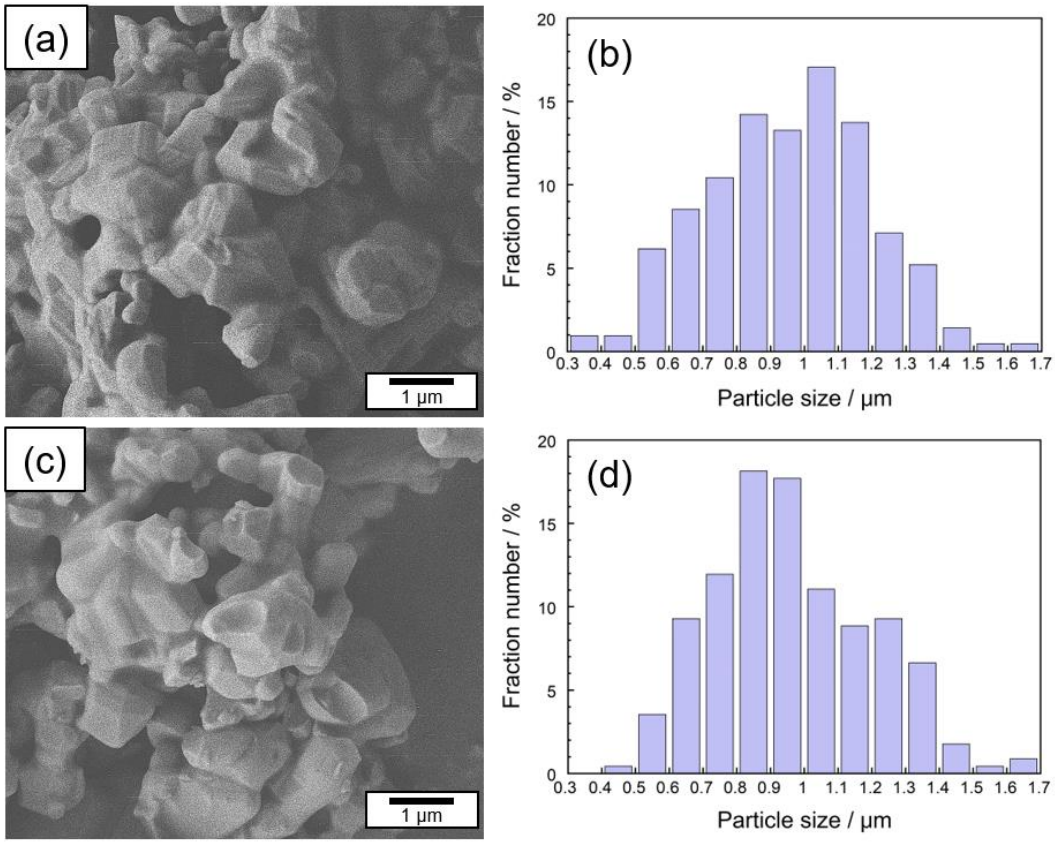

Figure 5.3 FE-SEM images and size distributions of $Ca_2Mn_{0.85}Ti_{0.15}O_4$ (a and b) and $Ca_2Mn_{0.77}Ti_{0.15}Zn_{0.08}O_{3.92}$ (c and d).

5.3.3 Reflectance spectra

Figure 5.4 (a) depicts the UV–Vis and NIR reflectance spectra of the $Ca_2Mn_{0.85-x}Ti_{0.15}Zn_xO_{4-x}$ ($0 \leq x \leq 0.10$) samples. All samples strongly absorbed visible light at a wavelength of 700 nm and shorter and reflected NIR light, due to small bandgap energies around 1.77 eV.[59] An enlarged view of the reflectance spectra from 300 to 750 nm was shown in **Figure 5.4 (b)**. Optical reflectance from 600 to 750 nm corresponding to the red light was decreased by the Zn^{2+} doping. As a result, the color of the samples changed from slightly reddish black to more vivid black and the redness of the samples was reduced.

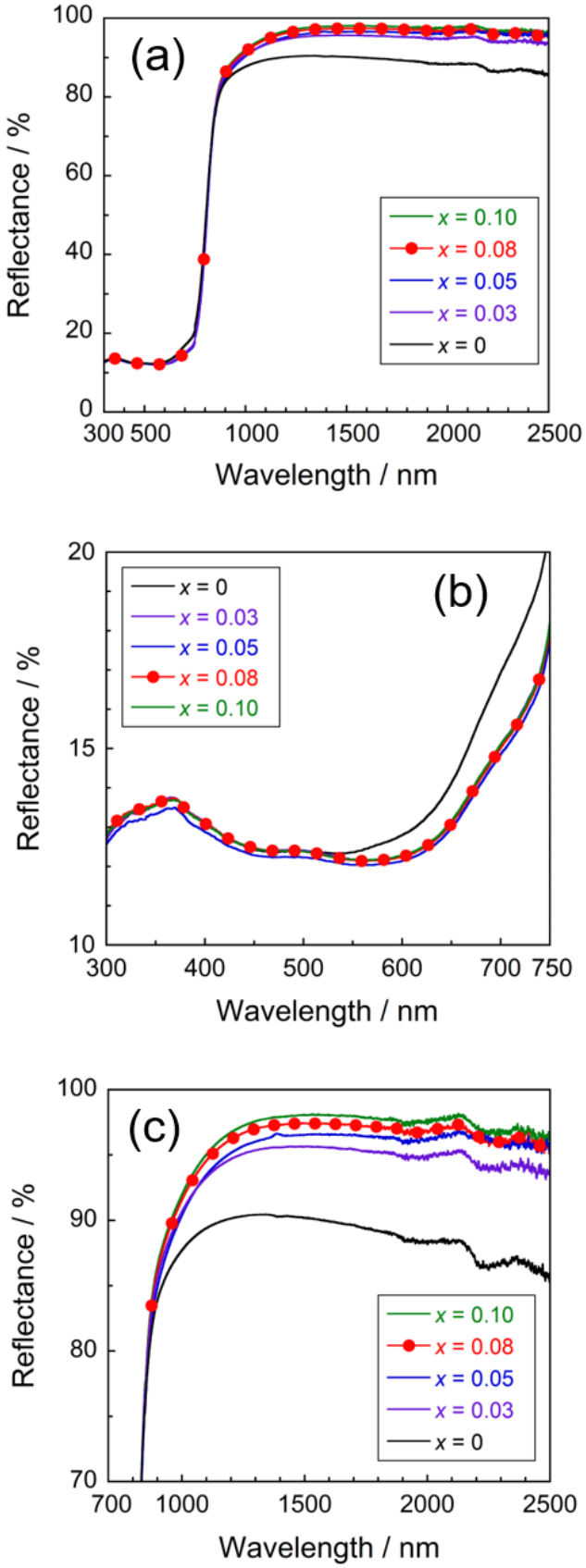

Figure 5.4 UV–Vis–NIR (a), UV–Vis (b), and NIR (c) reflectance spectra of the $Ca_2Mn_{0.85-x}Ti_{0.15}Zn_xO_{4-x}$ ($0 \leq x \leq 0.10$) samples.

As discussed above in **Table 5.1**, the [MnO_6] octahedron was significantly distorted by the dissolution of Zn^{2+}. This lattice distortion increased with increasing the Zn^{2+} concentration, and the symmetry of the [MnO_6] octahedron decreased. Thus, the reduction in red light reflection was caused by the d–d transition absorption of Mn^{4+}. This transition is essentially forbidden but has been partially allowed due to the loss of symmetry. On the other hand, the Mn^{4+} content of the sample was decreased by the Zn^{2+} substitution. In other words, enhancement of the optical absorption by Mn^{4+} in the red-light region and decrease of the amount of Mn^{4+} responsible for this absorption are in the relationship of trade-off. Accordingly, the optical reflectance in the red-light region almost unchanged in the range of $0.03 \leq x \leq 0.08$.

On the other hand, the optical reflectance in the NIR region was increased by the Zn^{2+} doping, as seen in **Figure 5.4 (c)**. The optical absorption in the NIR region was caused by the allowed charge transfer transition between Mn^{4+} and Mn^{3+} ions,[119] and this absorption intensity depended on the concentration of manganese. Unfortunately, it is difficult to confirm how much the CaO and ZnO impurity phases are involved in improving the NIR reflectivity. Since CaO and ZnO can strongly reflect the visible light as well as the NIR light, the optical reflectance in the visible light region shall also be increased by the Zn^{2+} doping, when the effect of these impurities is large. However, the reflectance in the visible light region did not increase, but rather the reflectance of red light decreased. Therefore, the increase in the NIR reflectivity is dominantly due to the decrease in manganese ions in the sample.

5.3.4 Chromatic properties and NIR solar reflectance

The color coordinate data and total (R_{Tot}) and NIR solar reflectance (R_{NIR}) of the $Ca_2Mn_{0.85-x}Ti_{0.15}Zn_xO_{4-x}$ ($0 \leq x \leq 0.10$) pigments are summarized in **Table 5.2**. The photographs of these pigments are also displayed in **Figure 5.5**. All pigments synthesized in this study showed low L^* values and were black as seen in **Figure 5.5**. The a^*, b^*, and C values of the Zn^{2+}-doped pigments were almost the same, but lower than those of the undoped $Ca_2Mn_{0.85}Ti_{0.15}O_4$ pigment ($x = 0$). As already discussed with respect to the results in **Figure 5.4 (b)**, this was due to the decrease in the optical reflectionin the red-light region (600–750 nm). The R_{NIR} value increased conversely with the Zn^{2+} doping, because the relative number of manganese ions decreased and the reflectance in the NIR region was increased as seen in **Figure 5.4 (a)** and **(c)**.

Table 5.2 Color coordinate data and total (R_{Tot}) and NIR (R_{NIR}) solar reflectance of the $Ca_2Mn_{0.85-x}Ti_{0.15}Zn_xO_{4-x}$ ($0 \leq x \leq 0.10$) pigments

x	L^*	a^*	b^*	C	R_{Tot} / %	R_{NIR} / %
0	24.4	+4.30	+2.72	5.09	43.7	71.7
0.03	23.2	+2.70	+0.72	2.79	44.6	73.8
0.05	22.1	+2.84	+0.94	2.99	44.5	73.7
0.08	23.2	+2.81	+0.83	2.93	45.0	74.6
0.10	23.3	+2.97	+0.94	3.12	45.3	75.1

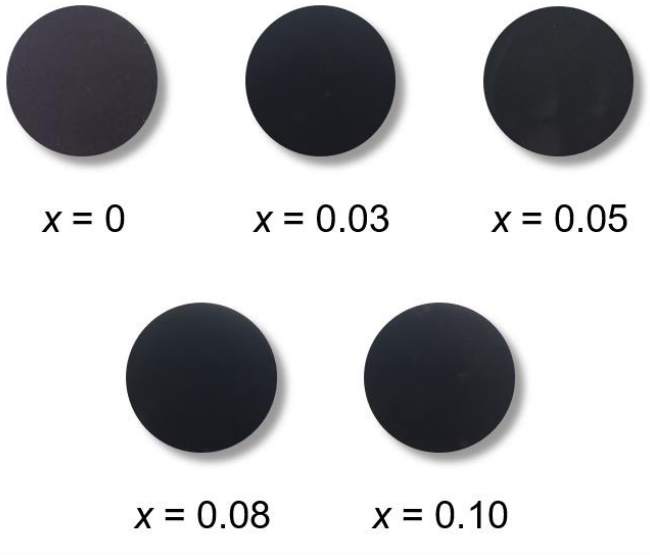

Figure 5.5 Photographs of the $Ca_2Mn_{0.85-x}Ti_{0.15}Zn_xO_{4-x}$ ($0 \leq x \leq 0.10$) pigments.

For an achromatic color such as black, the *C* value should be as small as possible in the *L*a*b*C* system. As recognized in the *C* and R_{NIR} values of the Zn^{2+}-doped samples in **Table 5.2**, the color tone became blacker and the NIR solar reflectance was improved. Among the $Ca_2Mn_{0.85-x}Ti_{0.15}Zn_xO_{4-x}$ ($0 \leq x \leq 0.08$) pigments synthesized in this study, $Ca_2Mn_{0.77}Ti_{0.15}Zn_{0.08}O_{3.92}$ showed a relatively low *C* value and the highest R_{NIR} value. Therefore, it was evidenced that $Ca_2Mn_{0.77}Ti_{0.15}Zn_{0.08}O_{3.92}$ has high performance as an inorganic black pigment with thermal barrier characteristics.

5.3.5 Comparison with commercially available pigments

The UV–Vis–NIR reflectance spectrum and the color parameters of the $Ca_2Mn_{0.77}Ti_{0.15}Zn_{0.08}O_{3.92}$ pigment was compared with those of the commercially available black pigments such as Black 6350 (iron and chromium oxide, Asahi Kasei), Black 6301

(manganese and bismuth oxide), MPT-370 (calcium, titanium, and manganese oxide, Ca(Ti, Mn)O_3, Ishihara Sangyo), and carbon black (Wako Chemical), as shown in **Figure 5.6** and summarized in **Table 5.3**. The photographs of these pigments are also displayed in **Figure 5.7**. As evidenced from these results, the present $Ca_2Mn_{0.77}Ti_{0.15}Zn_{0.08}O_{3.92}$ pigment showed higher reflectance in the NIR wavelength region and significantly higher R_{NIR} value than did the commercial pigments. Furthermore, the present pigment showed sufficiently low L^* and C values, similar to the commercially available NIR-reflective black pigments.

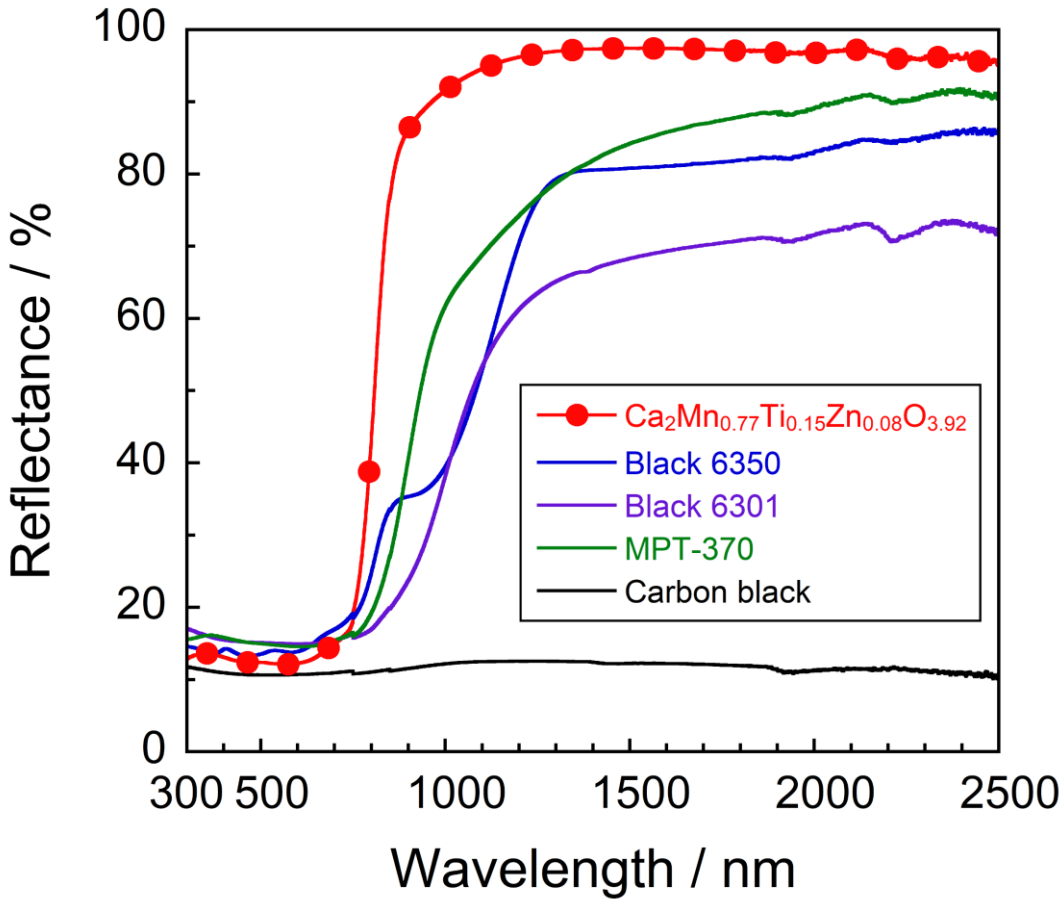

Figure 5.6 UV–Vis–NIR reflectance spectra of various black pigments.

Table 5.3 Color coordinate data and total (R_{Tot}) and NIR (R_{NIR}) solar reflectance of the black pigments

Pigment	*L**	*a**	*b**	*C*	R_{Tot} / %	R_{NIR} / %
$Ca_2Mn_{0.77}Ti_{0.15}Zn_{0.08}O_{3.92}$	23.2	+2.81	+0.83	2.93	45.0	74.6
Black 6350	26.4	+0.93	+4.19	4.29	31.7	47.8
Black 6301	24.0	+0.77	+1.14	1.38	28.3	40.3
MPT-370	25.1	+0.90	−0.41	0.99	34.5	52.3
Carbon black	2.69	+0.98	+1.90	2.14	11.3	11.7

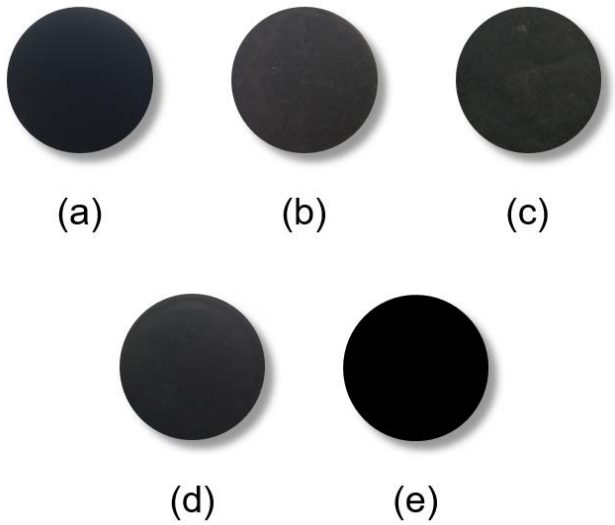

Figure 5.7 Photographs of $Ca_2Mn_{0.77}Ti_{0.15}Zn_{0.08}O_{3.92}$ (a), Black 6350 (b), Black 6301 (c), MPT-370 (d), and carbon black (e).

5.3.6 Chemical stability test

The chemical stability of the $Ca_2Mn_{0.77}Ti_{0.15}Zn_{0.08}O_{3.92}$ pigment was also evaluated. The powder sample was soaked into 4% acetic acid and 4% ammonium bicarbonate aqueous solutions. After leaving them at room temperature for 24 h, the samples were washed with deionized water and ethanol, and then dried at room temperature. The NIR-reflectance properties and color of the samples after the chemical stability test was evaluated using the

UV–Vis–NIR spectrometer and the colorimeter. Unfortunately, the color degradation and the decrease of the R_{Tot} and R_{NIR} values were observed by leaching the sample in both acetic acid and basic ammonium carbonate solutions, as seen in **Table 5.4**. Therefore, it is suggested that surface coating with a stable compound such as silica is necessary to suppress the deterioration.

Table 5.4 Color coordinates and total (R_{Tot}) and NIR (R_{NIR}) solar reflectance of $Ca_2Mn_{0.77}Ti_{0.15}Zn_{0.08}O_{3.92}$ before and after chemical stability test

Treatment	L^*	a^*	b^*	C	R_{Tot} / %	R_{NIR} / %
None	23.2	+2.81	+0.83	2.93	45.0	74.6
4% CH_3COOH	16.0	+10.6	+3.33	11.1	39.4	63.8
4% NH_4HCO_3	23.6	+4.76	+4.32	6.43	44.4	73.0

5.4 Conclusion

$Ca_2Mn_{0.85-x}Ti_{0.15}Zn_xO_{4-x}$ solid solutions were synthesized as NIR-reflective black pigments to improve the blackness of a $Ca_2Mn_{0.85}Ti_{0.15}O_4$ pigment without decreasing the NIR reflectance. By the introduction of Zn^{2+} in the $Ca_2Mn_{0.85}Ti_{0.15}O_4$ lattice, the reflection of the red-light (600–750 nm) was decreased due to the enhancement of the d–d transition of Mn^{4+}, while the NIR reflectance was increased by the decrease of the charge transfer transition between Mn^{4+} and Mn^{3+}. As a result, the black color tone of the non-doped $Ca_2Mn_{0.85}Ti_{0.15}O_4$ pigment was improved by the Zn^{2+} doping, and the highest NIR solar reflectance value (R_{NIR} = 74.6%) was observed at the composition of $Ca_2Mn_{0.77}Ti_{0.15}Zn_{0.08}O_{3.92}$. Furthermore, the

present pigment exhibited enough black color and the NIR reflectance ability is significantly higher than those of the conventional commercially available black pigments (R_{NIR} < 53.0%). Although it is necessary to improve the chemical stability, the $Ca_2Mn_{0.77}Ti_{0.15}Zn_{0.08}O_{3.92}$ pigment has a potential to be an inorganic black pigment for thermal shielding.

Chapter 6

Summary

In the work of this thesis, novel environment-friendly inorganic warm-colored and NIR-reflective black pigments have been successfully synthesized. Their color properties were characterized to produce advanced coloring materials with high performance. The results obtained through this work are summarized as follows:

< **Chapter 2** >

Novel environmentally friendly inorganic orange pigments, $Ca_{14}(Al_{1-x}Fe_x)_{10}Zn_6O_{35}$ ($0 \leq x \leq 0.30$), were synthesized using a solid-state reaction method. The Fe^{3+}-doped samples strongly absorbed visible light at wavelengths from 380 to 490 nm due to the d–d ($^6A_1 \rightarrow {}^4E$) transition of Fe^{3+}. In addition, the optical absorption around 600 nm, corresponding to the $^6A_1 \rightarrow {}^4T_2$ transition of Fe^{3+}, also increased with increasing the Fe^{3+} concentration. The sample color gradually turned from yellow to orange as the Fe^{3+} content increased. The most vivid orange color was obtained for the $Ca_{14}(Al_{0.85}Fe_{0.15})_{10}Zn_6O_{35}$ pigment. In addition, the thermal stability of this pigment was higher than that of commercial Bayferrox® 960 pigment.

< **Chapter 3** >

Ta^{5+}-doped Bi_2O_3 solid solutions, $(Bi_{1-x}Ta_x)_2O_{3+2x}$ ($0 \leq x \leq 0.20$), were synthesized by a conventional solid-state reaction method. The crystal system of the $(Bi_{1-x}Ta_x)_2O_{3+2x}$ ($0 \leq x \leq$

0.20) samples depended on the Ta^{5+} content, and, among them, the tetragonal $(Bi_{0.97}Ta_{0.03})_2O_{3.06}$ sample exhibited the most vivid orange color. Additionally, this work elucidates that the average Bi–O bond distance in the crystal lattice was short in the order of the tetragonal $(Bi_{0.97}Ta_{0.03})_2O_{3.06}$, the cubic $(Bi_{0.80}Ta_{0.20})_2O_{3.40}$, and the monoclinic Bi_2O_3 samples, and as a result, the bandgap energy became smaller and the light absorption wavelength became longer in the same order.

< **Chapter 4** >

$(Li_{1-x}Na_x)_2MnO_3$ ($0 \leq x \leq 0.10$) solid solutions were synthesized by a conventional solid-state reaction technique to investigate the relationship between the steric structure of the $[MnO_6]$ octahedra and coloration mechanisms. From the results of Rietveld analysis, it has been elucidated that the average Mn(2)–O bond length was increased and the $[Mn(2)O_6]$ octahedra were distorted by the Na^+ doping. As a result, the optical absorption band in the green light region shifted to the longer wavelength side due to the decrease in the crystal field around Mn^{4+} caused by the increase in the bond length. On the other hand, the red-light reflection was reduced by the distortion of the $[Mn(2)O_6]$ octahedra. In response to these phenomena, the color of $(Li_{1-x}Na_x)_2MnO_3$ turned from orange to deep red by increasing the Na^+ content. This study elucidates that the coordination environment around Mn^{4+} is one of the important factors to control the color of $(Li_{1-x}Na_x)_2MnO_3$.

< **Chapter 5** >

Inorganic black pigments with thermal barrier characteristics, $Ca_2Mn_{0.85-x}Ti_{0.15}Zn_xO_{4-x}$ ($0 \leq x \leq 0.10$), were synthesized using a conventional solid-state reaction method in order to improve the blackness without decreasing the near-infrared (NIR) reflectance of a $Ca_2Mn_{0.85}Ti_{0.15}O_4$ pigment, which was previously reported by our group. This work elucidated that an advanced $Ca_2Mn_{0.77}Ti_{0.15}Zn_{0.08}O_{3.92}$ pigment exhibited significantly larger NIR reflectance value (R_{NIR} = 74.6%) than those of the commercially available pigments (R_{NIR} < 53.0%). In addition, the present work elucidated that control of the geometric structure around Mn^{4+} and the charge transfer transition between Mn^{4+} and Mn^{3+} in the $Ca_2Mn_{0.85}Ti_{0.15}O_4$ lattice was possible by the introduction of Zn^{2+}, and, as a result, both sufficient black color tone and high NIR reflectance were realized simultaneously.

Acknowledgements

The author would like to express his heartfelt gratitude to Professor Dr. Toshiyuki Masui at Department of Chemistry and Biotechnology, Graduate School of Engineering, Tottori University, for his continuous guidance, many invaluable suggestions, his science encouragement throughout the work, and for his advice to my private life.

The author is deeply grateful to Professor Dr. Hiroki Sakaguchi, Department of Chemistry and Biotechnology, Graduate School of Engineering, Tottori University, and Professor Dr. Naonobu Katada, Department of Chemistry and Biotechnology, Graduate School of Engineering, Tottori University, for reviewing this thesis and giving their valuable comments.

Special thanks should be given to the author's co-workers, Mr. Takashi Tsukimori, Mr. Fumiya Aoyama, Mr. Hiroki Inoue, Mr. Yusuke Shobu, Mr. Kohei Kusukami, Mr. Takashi Kosaya, and Ms. Senri Iwasaki, and all other members of the research group under direction of Professor Toshiyuki Masui, Tottori University.

This work was partially supported by the JSPS KAKENHI grant number 19K05668 and the JSPS research Fellow (No. 201823369).

Finally, the author gratefully thanks to his father, Akiyoshi Oka, his mother, Miho Oka, his elder sister, Naomi Oka, and his younger brother, Kenta Oka.

References

1) G. Buxbaum, G. Pfaff, Industrial Inorganic Pigments, Wiley–VCH (2005).

2) E. B. Faulkner, R. J. Schwartz, High Performance Pigments 2nd ed., Wiley–VCH (2009).

3) M. Jansen, H. P. Letschert, *Nature*, **404**, 980 (2000).

4) S. Zhang, M. Ye, S. Chen, A. Han, Y. Zang, *Ceram. Int.*, **42**, 16023 (2016).

5) S. Liu, Y. Li, Z. Wang, Z. Shen, Z. Xie, *Appl. Surf. Sci.*, **387**, 1147 (2016).

6) P. Maestro, D. Huguenin, *J. Alloys Compd.*, **225**, 520 (1995).

7) S. Radhika, K. J. Sreeram. B. U. Nair, *J. Chem. Sci.*, **126**, 65 (2014).

8) L. S. Kumari, G. George, P. P. Rao, M. L. P. Reddy, *Dyes Pigm.*, **77**, 427 (2008).

9) P. Jiang, J. Li, A. W. Sleight, M. A. Subramanian, *Inorg. Chem.*, **50**, 5858 (2011).

10) L. S. Kumari, P. P. Rao, S. Sameera, P. Koshy, *Ceram. Int.*, **38**, 4009 (2012).

11) M. Llusar, E. García, M. T. García, C. Gargori, J. A. Badenes, G. Monrós, *J. Eur. Ceram. Soc.*, **35**, 357 (2015).

12) Wendusu, T. Yoshida, T. Masui, N. Imanaka, *J. Adv. Ceram.*, **4**, 39 (2015).

13) K. Kusumoto, *J. Ceram. Soc. Jpn.*, **124**, 926 (2016).

14) M. Shirpour, M. A. F. Sani, A. Mirhabibi, *Ceram. Int.*, **33**, 1427 (2007).

15) B. Bae, N. Takeuchi, S. Tamura, N. Imanaka, *Dyes Pigm.*, **147**, 523 (2017).

16) S. Tamilarasan, S. Laha, S. Ntarajan, J. Gopalakrishnan, *Eur. J. Inorg. Chem.*, **2**, 288 (2016).

17) Wendusu, A. Shiraishi, N. Takeuchi, T. Masui, N. Imanaka, *RSC Adv.*, **5**, 44886 (2015).

18) G. Giampaoli, J. Li, R. P. Hermann, J. K. Stalick, M. A. Subramanian, *Solid State Sci.*, **81**, 32 (2018).

19) J. Chen, Y. Xiao, B. Huang, X. Sun, *Dyes Pigm.*, **154**, 1 (2018).

20) Wendusu, T. Masui, N. Imanaka, *J. Asian Ceram. Soc.*, **2**, 195 (2014).

21) D. Schildhammer, G. Fuhrmann, L. Petschnig, N. Weinberger, H. Schottenberger, H. Huppertz, *Dyes Pigm.*, **138**, 90 (2017).

22) R. G. Rao, D. Divya, *Asian J. Chem.*, **29**, 1673 (2017).

23) K. Kusumoto, *J. Ceram. Soc. Jpn.*, **125**, 396 (2017).

24) D. Schildhammer, G. Fuhrmann, L. Petschnig, H. Schottenberger, H. Huppertz, *Dyes Pigm.*, **140**, 22 (2017).

25) L. Stránská, P. Šulcová, M. Vlček, *J. Therm. Anal. Calorim.*, **113**, 127 (2013).

26) L. Strnadlová, P. Šulcová, M. Llusar, *J. Therm. Anal. Calorim.*, **102**, 661 (2010).

27) P. Šulcová, M. Trojan, *J. Therm. Anal. Calorim.*, **83**, 557 (2006).

28) P. Šulcová, M. Trojan, *J. Therm. Anal. Calorim.*, **88**, 111 (2007).

29) G. Gramm, G. Fuhrmann, M. Wieser, H. Schottenberger, H. Huppertz, *Dyes Pigm.*, **160**, 9 (2019).

30) A. K. V. Raj, P. P. Rao, T. S. Sreena, *ACS Sustainable Chem. Eng.*, **7**, 8804 (2019).

31) M. Jovaní, A. Sanz, H. Beltrán-Mir, E. Cordoncillo, *Dyes Pigm.*, **133**, 33 (2016).

32) H. Saal, M. Binnewies, M. Schrader, A. Börger, K.-D. Becker, V. A. Tikhomirov, K. Jug, *Chem. Eur. J.*, **15**, 6408 (2009).

33) S. W. Kim, T. Hasegawa, M. Watanabe, K. Sugimoto, Y. Saito, K. Uematsu, K. Toda, M. Sato, *Dyes Pigm.*, **136**, 219 (2017).

34) G. George, P. P. Rao, M. L. Reddy, *Chem. Lett.*, **35**, 1412 (2006).

35) H. Hashimoto, M. Nakanishi, H. Asaoka, T. Maeda, Y. Kusano, T. Fujii, J. Takeda, *ACS Appl. Mater. Interfaces*, **6**, 20282 (2014).

36) M. Fortuño-Morte, H. Beltrán-Mir, E. Cordoncillo, *J. Alloys Compd.*, **845**, 155841 (2020).

37) S. Divya, S. Das, *Opt. Mater.*, **109**, 110410 (2020).

38) H. Akbari, Urban Heat Islands: Consequences and Mitigation Measures, Springer (2015).

39) R. Levinson, P. Berdahl, H. Akbari, *Sol. Energy Mater. Sol. Cells*, **89** 319 (2005).

40) B. Kaur, N. Quanzi, I. Ivanov, S. N. Bhattacharya, *Dyes Pigm.*, **92**, 1108 (2012).

41) Y. Shi, M. Zhong, Z. Zhang, D. Wang, *Ceram. Int.*, **43**, 5979 (2017).

42) H. Huang, Y. Xiao, H. Zhou, J. Chen, X. Sun, *ACS Sustainable Chem. Eng.*, **6**, 10735 (2018).

43) C. Ding, A. Han, M. Ye, Y. Zhang, L. Yao, J. Yang, *RSC Adv.*, **8**, 19690 (2018).

44) T. R. A. Thara, P. P. Rao, A. K. V. Raj, T. S. Sreena, *Sol. Energy Mater. Sol. Cells*, **200**, 110015 (2019).

45) S. F. Sameera, P. P. Rao, L. S. Kumari, V. James, S. Divya, *Chem. Lett.*, **42**, 521 (2013).

46) S. Jose, S. B. Narendranath, N. V. Sajith, M. R. P. Kurup, P. Periyat, *Matter. Lett.*, **233**, 82 (2018).

47) B. Huang, Y. Xiao, C. Huang, J. Chen, X. Sun, *Dyes Pigm.*, **147**, 225 (2017).

48) P. K. Thejus, B. Koley, K. G. Nishanth, *Dyes Pigm.*, **158**, 267 (2018).

49) E. A. Chaverriaga, A. A. Lopera, T. B. Wermuth, O. J. Restrepo, C. P. Bergmann, *Dyes Pigm.*, **157**, 1 (2018).

50) A. K. V. Raj, P. P. Rao, S. Divya, T. R. Ajuthara, *Powder Technol.*, **311**, 52 (2017).

51) J. Jing, Y. Zhang, J. Sun, X. Zhao, D. Gao, Y. Zhang, *Dyes Pigm.*, **150**, 9 (2018).

52) M. Cai, S. Chen, X. Ma, J. Chen, *J. Rare Earth*, **37**, 741 (2019).

53) J. O. Primo, K. W. Borth, D. C. Peron, V. C. Teixeira, D. Galante, C. Bittencourt, F. J. Anaissi, *J. Alloys Compd.*, **780**, 17 (2019).

54) R. Levinson, P. Berdahl, H. Akbari, *Sol. Energy Mater. Sol. Cells*, **89**, 351 (2005).

55) R. Levinson, P. Berdahl, H. Akbari, W. Miller, I. Joedicke, J. Reilly, Y. Suzuki, M. Vondran, *Sol. Energy Mater. Sol. Cells*, **91**, 304 (2007).

56) S. Jose, D. Joshy, S. B. Narendranath, P. Periyat, *Sol. Energy Mater. Sol. Cells*, **194**, 7 (2019).

57) A. Han, M. Zhao, M. Ye, J. Liao, Z. Zhang, N. Li, *Sol. Energy*, **91**, 32 (2013).

58) A. Han, M. Ye, M. Zhao, J. Liao, T. Wu, *Dyes Pigm.*, **99**, 527 (2013).

59) R. Oka, T. Masui, *RSC Adv.*, **6**, 90952 (2016).

60) Ž. Dohnalová, P. Šulcová, P. Bělina, M. Vlček, N. Gorodylova, *J. Therm. Anal. Calorim.*, **133**, 421 (2018).

61) R. Radha, A. Srinivasan, P. Manimuthu, S. Balakumar, *J. Mater. Chem. C*, **3**, 10285 (2015).

62) D. Wang, D. Su, M. Zhong, *Sol. Energy*, **110**, 1 (2014).

63) F. G. Maranha, T. E. R. Fiuza, E. C. F. de Souza, J. F. M. Borges, J. B. M. da Cunha, A. V. C. de Andrade, S. R. M. Antunes, A. C. Antunes, *Dyes Pigm.*, **133**, 304 (2016).

64) H. Liu, L. Yuan, H. Qi, S. Wang, Y. Du, Y. Zhang, C. Hou, S. Feng, *Dyes Pigm.*, **145**, 418 (2017).

65) J. Chen, W. Zhao, N. Wang, Y. Meng, S. Yi, J. He, X. Zhang, *J. Mater. Sci.*, **51**, 4201 (2016).

66) X. Gao, W. Li, X. Yang, X. Jin, S. Xiao, *J. Phys. Chem. C*, **119**, 28090 (2015).

67) T. Hasegawa, S. W. Kim, T. Abe, S. Kumagai, R. Yamanashi, K. Seki, K. Uematsu, K. Toda, M. Sato, *Chem. Lett.*, **45**, 1096 (2016).

68) W. Lü, W. Lv, Q. Zhao, M. Jiao, B. Shao, H. You, *Inorg. Chem.*, **53**, 11985 (2014).

69) R. D. Shannon, *Acta Cryst.*, **A32**, 751 (1976).

70) R. Oka, T. Kosaya, T. Masui, *Chem. Lett.*, **47**, 1522 (2018).

71) V. D. Barbanyagre, T. I. Timoshenko, A. M. Ilyinets, V. M. Shamshurov, *Powder Diffr.*, **12**, 22 (1997).

72) A. K. Zak, M. E. Abrishami, W. H. A. Majid, R. Yousefi, S. M. Hosseini, *Ceram. Int.*, **37**, 393 (2011).

73) B. Bradley, M. Singleton, A. L. W. Po, *J. Clin. Pharm. Ther.*, **14**, 423 (1989).

74) K. A. Winship, *Adverse Drug React. Acute Poisoning Rev.*, **2**, 103 (1983).

75) W. J. Serfontein, R. Mekel, *Res. Commun. Chem. Pathol. Pharmacol.*, **26**, 391 (1979).

76) N. M. Sammes, G. A. Tompsett, H. Näfe, F. Aldinger, *J. Eur Ceram. Soc.*, **19**, 1801 (1999).

77) L. Zhang, W. Wang, J. Yang, Z. Chen, W. Zhang, L. Zhou, S. Liu, *Appl. Catal. A Gen.*, **308**, 105 (2006).

78) H. Cheng, B. Huang, J. Lu, Z. Wang, B. Xu, X. Qin, X. Zhang, Y. Dai, *Phys. Chem. Chem. Phys.*, **12**, 15468 (2010).

79) F. Wang, K. Cao, Q. Zhang, X. Gong, Y. Zhou, *J. Mol. Model.*, **20**, 2506 (2014).

80) Q.-Y. Li, Z.-Y. Zhao, *Phys. Lett. A*, **379**, 2766 (2015).

81) L. Li, L. Meng, F. Wang, Y. Wang, *Mater. Sci. Semicond. Process.*, **68**, 48 (2017).

82) T. Takahashi, H. Iwahara, T. Esaka, *J. Electrochem. Soc.*, **124**, 1563 (1977).

83) T. Takahashi, H. Iwahara, *Mater Res. Bull.*, **13**, 1447 (1978).

84) H. Iwahara, T. Esaka, T. Sato, T. Takahashi, *J. Solid State Chem.*, **39**, 173 (1981).

85) M. Ahila, E. Subramanian, P. D. Pathinettam, *Ionics*, **24**, 1827 (2018).

86) M. Manjula, B. Karthikeyan, D. Sastikumar, *Opt. Fiber Technol.*, **45**, 35 (2018).

87) S. K. Blower, C. Geaves, *Acta Cryst.*, **C44**, 587 (1988).

88) P. Kubelka, F. Munk, *Z. Tech. Phys.*, **12**, 593 (1931).

89) S. Hull, S. T. Norberg, M. G. Tucker, S. G. Eriksson, C. E. Mohn, S. Stølen, *Dalton Trans.*, 8737 (2009).

90) R. A. Evarestov, V. O. Shapovalov, V. A. Veryazov, *Phys. Status Solidi B*, **183**, K15 (1994).

91) Wendusu, K. Ikawa, T. Masui, N. Imanaka, *Chem. Lett.*, **40**, 792 (2011).

92) T. Masui, T. Honda, Wendusu, N. Imanaka, *Dyes Pigm.*, **99**, 636 (2013).

93) S. Ke, Y. Wang, Z. Pan, *Dyes Pigm.*, **118**, 145 (2015).

94) L. Qin, S. Bi, P. Cai, C. Chen, J. Wang, S. I. Kim, Y. Huang, H. J. Seo, *J. Alloys Compd.*, **755**, 61 (2018).

95) U. B. Humayoun, S. N. Tiruneh, D.-H. Yoon, *Dyes Pigm.*, **152**, 127 (2018).

96) Y. Zhu, Z. Qiu, B. Ai, Y. Lin, W. Zhou, J. Zhang, L. Yu, Q. Mi, S. Lian, *J. Lumin.*, **201**, 314 (2018).

97) T. Jansen, T. Jüstel, *J. Phys. Chem. Solids*, **110**, 180 (2017).

98) R. Cao, Y. Ye, Q. Peng, G. Zheng, H. Ao, J. Fu, Y. Guo, B. Guo, *Dyes Pigm.*, **146**, 14 (2017).

99) A. Fu, Q. Pang, H. Yang, L. Zhou, *Opt. Mater.*, **70**, 144 (2017).

100) F. Zheng, J. Zou, B. Yang, Y. Liu, H. Zhou, M. Shi, M. Li, X. Qian, Z. Liu, Y. Li, *J. Mater. Sci.: Mater. Electron.*, **29**, 21061 (2018).

101) T. Hasegawa, Y. Nishiwaki, F. Fujishiro, S. Kamei, T. Ueda, *ACS Omega*, **4**, 19856 (2019).

102) Z. Liu, M. Yuwen, J. Liu, C. Yu, T. Xuan, H. Li, *Ceram. Int.*, **43**, 5674 (2017).

103) S. Tamilarasan, S. Laha, S. Natarajan, J. Gopalakrishnan, *J. Mater. Chem. C*, **3**, 4794 (2015).

104) A. Gupta, S. Pal, S. Uma, *J. Phys. Chem. Solids*, **134**, 238 (2019).

105) F. Izumi, K. Momma, *Solid State Phenom.*, **130**, 15 (2007).

106) A. Boulineau, L. Croguennec, C. Delmas, F. Weill, *Chem. Mater.*, **21**, 5216 (2009).

107) A. Boulineau, L. Croguennec, C. Delmas, F. Weill, *Solid State Ionics*, **180**, 1652 (2010).

108) C. H. Lei, J. G. Wen, M. Sardela, J. Bareño, I. Petrov, S.-H. Kang, D. P. Abraham, *J. Mater. Sci.*, **44**, 5579 (2009).

109) Y. Nakao, K. Ozawa, Y. Nemoto, F. Uesugi, H. Fujii, T. Mochiku, *J. Ceram. Soc. Jpn.*, **123**, 589 (2015).

110) M. Tabuchi, Y. Nabeshima, T. Takeuchi, K. Tatsumi, J. Imaizumi, Y. Nitta, *J. Power Sources*, **195**, 834 (2010).

111) T, Matsunaga, H. Komatsu, K. Shimoda, T. Minato, M. Yonemura, T. Kamiyama, S. Kobayashi, T. Kato, T. Hirayama, Y. Ikuhara, H. Arai, Y. Ukyo, Y. Uchimoto, Z. Ogumi, *Chem. Mater.*, **28**, 4143 (2016).

112) K. Momma, F. Izumi, *J. Appl. Cryst.*, **44**, 1272 (2011).

113) X. Dong, Y. Xu, L. Xiong, X. Sun, Z. Zhang, *J. Power Sources*, **243**, 78 (2013).

114) W. H. Baur, *Acta Cryst.*, **B30**, 1195 (1974).

115) H. Kamimura, S. Sugano, Y. Tanabe, Ligand Field Theory and Its Applications, Shokabo (1987).

116) M. E. Leonowicz, K. R. Poeppelmeier, J. M. Longo, *J. Solid State Chem.*, **59**, 71 (1985).

117) E. A. Medina, J. Li, J. K. Stalick, M. A. Subramanian, *Solid State Sci.*, **52**, 97 (2016).

118) H. Taguchi, *Mater. Res. Bull.*, **36**, 1361 (2001).

119) N. N. Kovaleva, J. L. Gavartin, A. L. Shluger, A. V. Boris, A. M. Stoneham, *J. Exp. Theor. Phys.*, **94**, 178 (2002).

List of Publications

[1] Novel Environmentally Friendly Inorganic Orange Pigments Based on $Ca_{14}Al_{10}Zn_6O_{35}$

Ryohei Oka, Takashi Kosaya, and Toshiyuki Masui

Chemistry Letters, **47**, 1522–1525 (2018).

[2] Synthesis and Color Evaluation of Ta^{5+}-Doped Bi_2O_3

Ryohei Oka, Yusuke Shobu, and Toshiyuki Masui

ACS Omega, **4**, 7581–7585 (2019).

[3] Effect of $[MnO_6]$ Octahedra to the Coloring Mechanism of $(Li_{1-x}Na_x)_2MnO_3$

Ryohei Oka, Kohei Kusukami, and Toshiyuki Masui

ACS Omega, **5**, 13108–13114 (2020).

[4] Improvement of Near-Infrared (NIR) Reflectivity and Black Color Tone by Doping Zn^{2+} into the $Ca_2Mn_{0.85}Ti_{0.15}O_4$ Structure

Ryohei Oka, Senri Iwasaki, and Toshiyuki Masui

RSC Advances, **9**, 38822–38827 (2019).

Supplementary Publications

[1] Synthesis and Characterization of Black Pigments Based on Calcium Manganese Oxides for High Near-Infrared (NIR) Reflectance

Ryohei Oka and Toshiyuki Masui

RSC Advances, **6**, 90952–90957 (2016).

[2] Synthesis and Characterization of $Bi_4Zr_3O_{12}$ as an Environment-Friendly Inorganic Yellow Pigment

Takashi Tsukimori, Ryohei Oka, and Toshiyuki Masui

Dyes and Pigments, **139**, 808–811 (2017).

[3] Perovskite-Type $ALnO_3$ (A = Ca, Sr, Ba; Ln = Ce, Pr, Tb) Oxides as Environmentally Friendly Yellow Pigments

Ryohei Oka, Takashi Tsukimori, Hiroki Inoue, and Toshiyuki Masui

Journal of the Ceramic Society of Japan, **125**, 652–656 (2017).

[4] Synthesis and Characterisation of $SrY_{2-x}Ce_xO_4$ as Environmentally Friendly Reddish-Brown Pigments

Ryohei Oka, Yusuke Shobu, Fumiya Aoyama, Takashi Tsukimori, and Toshiyuki Masui

RSC Advances, **7**, 55081–55087 (2017).

[5] Synthesis and Characterisation of $Ba(Zn_{1-x}Co_x)_2Si_2O_7$ ($0 \leq x \leq 0.50$) for Blue-Violet Inorganic Pigments

Takashi Tsukimori, Yusuke Shobu, Ryohei Oka, and Toshiyuki Masui

RSC Advances, **8**, 9017–9022 (2018).

[6] Submicron-Sized Phosphors Based on Hexagonal Rare Earth Oxycarbonate for Near-Infrared Excitation and Emission
Mizuki Watanabe, Yasuhiro Sejima, Ryohei Oka, Shintaro Ida, and Toshiyuki Masui
Journal of Asian Ceramic Societies, **7**, 502–508 (2019).

[7] Enhancement of Near-Infrared Emission of Neodymium-Doped Monoclinic Gadolinium Phosphate Nanophosphors by Surface Coating with Calcium Phosphate
Mizuki Watanabe, Norifumi Yamamoto, Tomoaki Matsuo, Ryohei Oka, Shintaro Ida, and Toshiyuki Masui
Journal of Asian Ceramic Societies, **7**, 509–517 (2019).

[8] Synthesis and Characterization of $Ca_{1-x}Eu_xZrO_3$ as Environmentally Friendly Inorganic Yellow Pigments
Kohei Minagawa, Yuichi Nishiguchi, Ryohei Oka, and Toshiyuki Masui
ACS Omega, in press.

[9] Novel Environment-Friendly Inorganic Reddish-Brown Pigments with Ce^{3+} as a Coloring Source
Ryohei Oka and Toshiyuki Masui
Ceramics Japan, **53**, 449–452 (2018) [in Japanese].

[10] Environment-Friendly Inorganic Pigments
Ryohei Oka and Toshiyuki Masui
Bulletin of the Japan Electronic Materials Society, **49**, 2–5 (2018) [in Japanese].

[11] Environmentally Friendly Inorganic Pigments

Ryohei Oka and Toshiyuki Masui

Ceramics Japan, **55**, 598–601 (2020) [in Japanese].